TIVIT: TIME SERIES REPRESENTATIONS LIE HIDDEN IN PRETRAINED VISION TRANSFORMERS

Anonymous authors
Paper under double-blind review

ABSTRACT

Time series classification is a fundamental task in healthcare and industry, yet the development of time series foundation models (TSFMs) remains limited by the scarcity of publicly available time series datasets. In this work, we propose **Ti**me **Vi**sion **T**ransformer (**TiViT**), a framework that converts time series into images to leverage the representational power of frozen Vision Transformers (ViTs) pretrained on large-scale image datasets. TiViT achieves state-of-the-art performance on time series classification and anomaly detection benchmarks by utilizing the hidden representations of large OpenCLIP models. We explore the structure of TiViT representations and find that intermediate layers with high intrinsic dimension are the most effective for time series classification. Furthermore, we assess the alignment between TiViT and TSFM representation spaces and identify a strong complementarity, with additional performance gains achieved by combining their features. Finally, we provide theoretical and qualitative insights about the benefits of 2D patching for time series modeling with ViTs. Our findings reveal a new direction for reusing vision representations in a non-visual domain.

1 INTRODUCTION

Foundation models have disrupted the field of machine learning. Typically built upon the Transformer (Vaswani et al., 2017) architecture, they are trained on large-scale datasets to learn generalizable representations for a wide range of downstream tasks. Vision models like DINOv3 (Siméoni et al., 2025) can be applied in image classification or segmentation with minimal supervision. Vision language models (VLMs) such as CLIP (Radford et al., 2021) or SigLIP (Tschannen et al., 2025; Zhai et al., 2023) can even be transferred to new tasks without any supervision since they have learned to ground semantic concepts in natural language. VLMs have been increasingly applied in new domains, including audio (Dixit et al., 2024; Xie et al., 2024) and medicine (Zhang et al., 2024).

Time series capture critical information in healthcare, finance, and manufacturing. Inspired by the success of foundation models in natural language processing (NLP) and computer vision (CV), similar models have recently been developed for the analysis of time series, following two different approaches. The first one is to pretrain time series foundation models (TSFMs) in a self-supervised way (Ansari et al., 2024; Das et al., 2024; Feofanov et al., 2025; Goswami et al., 2024; Lin et al., 2023) using a large-scale real-world time series dataset. The second one is to repurpose foundation models from other domains, such as NLP (Jin et al., 2024; Zhou et al., 2023) and CV (Chen et al., 2024; Li et al., 2023b), for time series tasks. The idea behind this approach is to benefit from the vast amount of samples that large vision and language models are trained on, and which are often unavailable in the time series domain.

Adapting vision models to time series analysis is particularly compelling, since time series can be visualized as line plots, heatmaps, or spectrograms (Ni et al., 2025). TimesNet (Wu et al., 2023) has been trained end-to-end on heatmaps generated from time series, pretrained Masked Autoencoders have been applied in zero-shot time series forecasting (Chen et al., 2024), and pretrained SwinTransformers have been finetuned on line plots of irregularly sampled time series (Li et al., 2023b). However, these approaches are either restricted to the task of forecasting or require costly per-dataset training and finetuning. No prior work has shown that large vision and vision-language models trained on billions of images can be state-of-the-art in time series classification. Furthermore, there is no theoretical explanation yet for the effectiveness of 2D time series modeling.

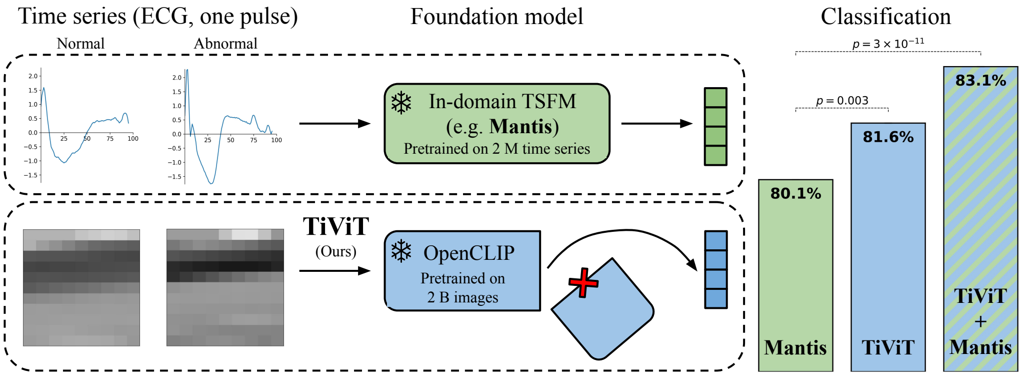

Figure 1: While TSFMs operate directly on the 1D time series signal, TiViT transforms time series into images to leverage pretrained ViTs for feature extraction. We display the average time series signal of two classes from ECG200 (Olszewski, 2001) and their corresponding 2D representations. Utilizing the hidden representations of OpenCLIP, TiViT significantly outperforms Mantis in linear classification on the UCR benchmark. Combining both models further improves accuracy.

In this work, we demonstrate that frozen vision foundation models such as OpenCLIP, SigLIP 2, and DINOv3, pretrained solely on natural images or image-text pairs, can serve as universal feature extractors for time series tasks without any pretraining or finetuning on time series data. The transformation of time series into images for feature extraction with ViTs is motivated by the intuition that 2D modeling spatially distributes label-relevant information across patches, thereby facilitating classification. To validate this hypothesis, we investigate 1D and 2D time series modeling with Transformers, offering insights into when and why image-based modeling can be advantageous.

Our main contributions are summarized as follows: (1) We introduce the Time Vision Transformer (TiViT), leveraging hidden representations of pretrained and frozen ViTs for time series analysis. TiViT surpasses conventional TSFMs without any fine-tuning in time series classification across 128 datasets and time series anomaly detection across 248 datasets. (2) We study the alignment of TiViTs and TSFMs and find that they extract complementary information from time series. By merging their representations, we achieve an average improvement of +3% over TSFMs in time series classification. (3) We provide a theoretical and empirical analysis at the patch level of Transformers, showing that the image-based modeling of time series reduces sample complexity and thus makes training more efficient than conventional 1D modeling.

2 RELATED WORK

Time series foundation models Recently, the research community has witnessed an impressive surge in the number and variety of TSFMs. At first, such models were based on repurposing large language models (LLMs) for time series tasks (Cao et al., 2024; Chang et al., 2025; Gruver et al., 2023; Jin et al., 2024; Xue & Salim, 2024; Zhou et al., 2023), exploiting the ability of LLMs to efficiently handle sequential data. A different approach that gained in popularity later was to train TSFMs from the ground up on extensive and diverse datasets (Ansari et al., 2024; Bhethanabhotla et al., 2024; Das et al., 2024; Feofanov et al., 2025; Gao et al., 2024; Goswami et al., 2024; Lin et al., 2023; Liu et al., 2024a;b; Rasul et al., 2024; Wang et al., 2024). While most of the models were designed for time series forecasting, several of them also specifically tackled time series classification (Feofanov et al., 2025; Gao et al., 2024; Goswami et al., 2024; Lin et al., 2023; Zhou et al., 2023). These TSFMs are on par with or exceed the performance of earlier deep learning models such as the famous TimesNet (Wu et al., 2023), which has been trained separately per dataset.

Transforming time series into images Time series can be transformed into images in many ways, either based on the 1D representation of the time series in the original space (line plot) or frequency space (spectrogram), or by using a 2D modeling approach (heatmap, Gramian angular field, recurrence plot) that stacks segments of the input time series based on a chosen periodicity. Vision models, often based on CNNs and their variations, were applied on such image-based representa-

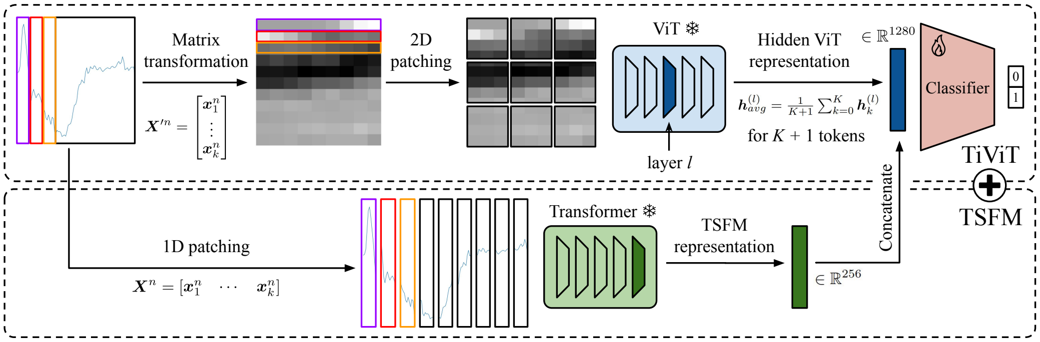

Figure 2: Illustration of TiViT on a time series sample from ECG200 (Olszewski, 2001). We split the time series into segments and stack them to form a grayscale image. Then, we patch the image in 2D and feed it into a frozen ViT pretrained on large-scale image datasets. We average the hidden representations from a specific layer and pass them to a learnable classification head. Concatenating the representations of TiViT and TSFMs prior to classification improves accuracy.

tions of time series as early as 2013 (see Ni et al. (2025) for a recent survey). Most of them, however, were trained in a supervised way to fit the dataset at hand. This work explores how pretrained vision models can be used as powerful feature extractors without training or fine-tuning. Li et al. (2023b) showed that pretrained ViTs can be effective in the classification of irregular time series from their line plot representations after full finetuning. In a similar vein, Chen et al. (2024) applied a masked auto-encoder with a pretrained frozen ViT to 2D transformed time series to perform time series forecasting. Different from these works, our TiViT model surpasses the performance of frontier TSFMs across a broad set of classification and anomaly detection benchmarks. Moreover, we explain why modeling time series in 2D rather than 1D can benefit time series classification with Transformers.

3 TiViT: Time Series Classification with Pretrained ViTs

We introduce the Time Vision Transformer (TiViT) leveraging pretrained frozen ViTs from the vision or vision-language domain for time series classification. We consider a multivariate time series dataset $\mathcal{T} = \{\boldsymbol{t}^n | \boldsymbol{t}^n \in \mathbb{R}^{T \times D}\}_{n=1}^{N}$ containing N samples, each of length T and dimensionality D. The corresponding targets $\mathcal{Y} = \{y^n\}_{n=1}^{N}$ are labels $y^n \in \{1, ..., C\}$ from C different classes. We transform the time series into images and apply ViTs on these images to extract representations for linear classification. Figure 2 illustrates our approach.

Time series-to-image transformation Following the channel independence assumption, proposed by Nie et al. (2023) and widely adopted in most recent TSFMs (Feofanov et al., 2025; Goswami et al., 2024), we first split a multivariate time series $\boldsymbol{t}^n \in \mathbb{R}^{T \times D}$ into D univariate time series $\{\boldsymbol{t}_d^n \in \mathbb{R}^{T}\}_{d=1}^{D}$. We then normalize each univariate time series $\boldsymbol{t}_d^n$ using robust scaling, defined as: $\frac{\boldsymbol{t}_d^n - Q_2}{Q_3 - Q_1}$, where Q_1, Q_2, Q_3 are the first, second (median), and third quartiles, respectively. We apply padding at the beginning of each time series by replicating its first value and subsequently segment it into M patches $\{\boldsymbol{x}_m\}_{m=1}^{M}$ of size P. Given a patch length P and stride S, the total number of patches is: $M = \left\lfloor \frac{T-P}{S} \right\rfloor + 1$. We stack the patches to generate a 2D representation $\boldsymbol{X}' \in \mathbb{R}^{M \times P}$, which we then render into a grayscale image $\boldsymbol{X}' \in \mathbb{R}^{M \times P \times 3}$ by replicating its signals across three channels. To align with the square input resolution (R, R) expected by the ViT, we resize the image.

Time series classification We feed each grayscale image $\boldsymbol{X}'$ representing a univariate time series into a pretrained and frozen ViT v with L hidden layers. The ViT inherent 2D patching yields a sequence $\{\boldsymbol{x}'_k \in \mathbb{R}^{U^2}\}_{k=1}^{K}$ of flattened patches where (U, U) is the resolution per patch and $K = R^2/U^2$ is the resulting number of patches. ViTs generally prepend a classification token to this sequence. The ViT consumes all input tokens and produces a sequence of features at every layer: $v(\boldsymbol{X}') = \left\{ [\boldsymbol{h}_0^{(l)}, \boldsymbol{h}_1^{(l)}, ..., \boldsymbol{h}_K^{(l)}] \right\}_{l=0}^{L}$. To obtain a single embedding vector $\boldsymbol{e}$ per image, we select a specific layer l and average its $K+1$ representations: $\boldsymbol{e} = \boldsymbol{h}_{avg}^{(l)} = \frac{1}{K+1} \sum_{k=0}^{K} \boldsymbol{h}_k^{(l)}$. For multivariate time series, we feed per-channel image representations $\{\boldsymbol{X}'_d\}_{d=1}^{D}$ separately into the ViT and concatenate the resulting embeddings for a specified layer: $\text{Concat}(\boldsymbol{e}_1, ..., \boldsymbol{e}_D)$. We only train a linear classifier on the ViT representations and their corresponding class labels. To enhance performance, the embeddings of frozen TSFMs and ViTs can be concatenated prior to classification.

4 EXPERIMENTAL EVALUATION

In this section, we evaluate TiViT on the discriminative time series tasks of classification and anomaly detection, showing its state-of-the-art performance compared to supervised, self-supervised, and FM competitors. Although the contrastive pre-training ViTs rely on is not suitable for generative tasks, we further provide promising preliminary results with TiViT in long-term multivariate forecasting. We note that classification and forecasting are two fundamentally different tasks, and most existing TSFMs concentrate exclusively on only one of them.

For classification, we evaluate TiViT on 128 univariate time series dataset from the UCR benchmark (Dau et al., 2019) and on 27 multivariate datasets from the UEA benchmark (Bagnall et al., 2018). Our study examines three differently pretrained ViTs: OpenCLIP (Cherti et al., 2023; Ilharco et al., 2021), SigLIP 2 (Tschannen et al., 2025), and DINOv3 (Siméoni et al., 2025). We compare TiViT to the state-of-the-art TSFMs Mantis (Feofanov et al., 2025) and Moment (Goswami et al., 2024) which are exclusively pretrained on time series. We further consider GPT4TS (Zhou et al., 2023) pretrained on textual data, the forecasting TSFMs VisionTS (Chen et al., 2024) and Chronos (Ansari et al., 2024), and a wide range of (self-)supervised baselines (pre-)trained per time series dataset. To evaluate the effectiveness of TiViT and TSFM representations in time series classification, we train a logistic regressor with the LBFGS solver per dataset. A detailed overview of our experimental setup is provided in Appendix C.

4.1 TRANSFORMING TIME SERIES INTO IMAGES FOR FEATURE EXTRACTION

The performance of our time series-to-image transformation is sensitive to the patch size P, as extreme values can create redundant visual tokens during resizing to the ViT input resolution (see Figure 10). To avoid a computationally expensive hyperparameter search for the optimal patch size P^* per dataset, we propose the heuristic $P = \sqrt{T}$ for any series of length T. This choice yields a square-shaped matrix representation prior to resizing, which minimizes horizontal or vertical distortion and thus preserves patch diversity. While an exhaustive search for P^* offers a marginal accuracy improvement in the case of no overlap, our heuristic provides a strong baseline at a fraction of the computational cost. As displayed in Figure 3, introducing overlap between patches further boosts performance and makes the impact of the optimal patch size vanish. Details can be found in Appendix D.1. Consequently, we use a patch size of $P = \sqrt{T}$ and a stride of $S = P/10$ in the following experiments.

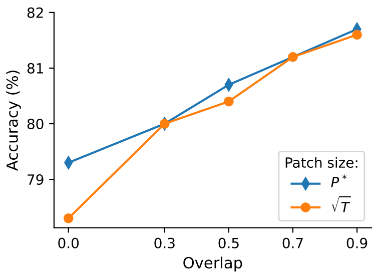

Figure 3: Effect of patch size and overlap on classification accuracy.

4.2 EFFECTIVENESS OF HIDDEN VIT REPRESENTATIONS

We repurpose frozen ViTs as feature extractors for time series data. While the final representations of ViTs typically capture high level semantics, intermediate layers encode lower level information (Dorszewski et al., 2025). Our study reveals that the intermediate representations of ViTs are the most effective for downstream classification. In Figure 4a we report the classification performance of TiViT with pretrained ViTs from DINOv3, CLIP, and SigLIP 2 on the validation split of the UCR benchmark. For each dataset, we extract representations from the hidden layers of ViTs, average them, and train a linear classifier. The intermediate representations of ViTs, between 40% and 70% of the layer depth, achieve the highest classification accuracy. CLIP and SigLIP 2, both optimized with a contrastive loss on image-text pairs, reach best performance in their earlier layers: layer 14 of 33 for CLIP (ViT-H) and layer 12 of 28 for SigLIP 2 (SoViT-400m). In contrast, DINOv3 (ViT-L) trained with contrastive learning and masked modeling on images only, reaches the highest

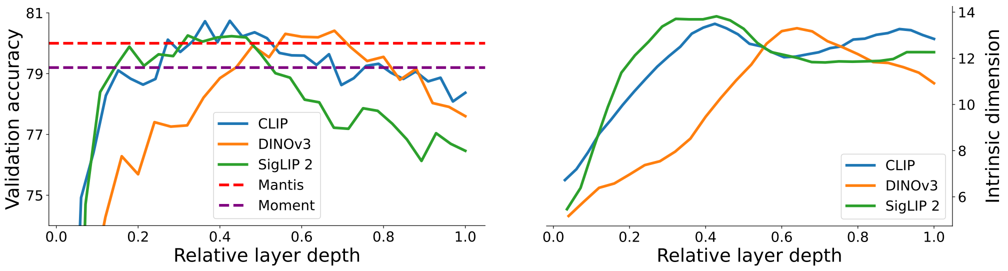

(a) Validation accuracy (b) Intrinsic dimension

Figure 4: (a) Validation accuracy and (b) Intrinsic dimensionality using hidden representations at different depth of pretrained ViTs (CLIP, DINOv3, SigLIP 2). Results are averaged over 128 datasets from the UCR benchmark.

Table 1: Classification accuracy of TSFMs and TiViT per benchmark.

Model	UCR	UEA
Moment	79.0	69.9
Mantis	80.1	72.4
TiViT *(Ours)*	81.6 +1.5	72.0 -0.4
TiViT + Moment *(Ours)*	82.7 +2.6	72.6 +0.2
TiViT + Mantis *(Ours)*	**83.1** +3.0	**73.7** +1.3

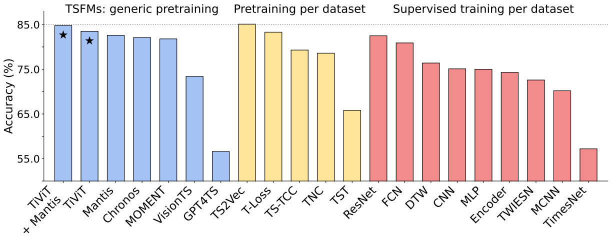

Figure 5: Classification accuracy across 91 UCR datasets. SL and SSL baselines from Goswami et al. (2024).

classification accuracy with representations from a later layer (17 of 25). For each ViT, we determine the optimal hidden layer based on its highest validation accuracy on the UCR benchmark.

Intrinsic dimension To better understand the hidden representations of ViTs, we analyze their intrinsic dimension (see Figure 4b) and principal components (see Appendix D.5). Valeriani et al. (2023) have previously investigated the geometry of hidden representations of Transformers for in-domain vision and language applications. We measure the intrinsic dimension of ViTs applied on time series from the UCR archive using the DADApy (Glielmo et al., 2022) implementation of the TWO-NN estimator (Facco et al., 2017). Figure 4b displays for three different ViT backbones the intrinsic dimensionality of their representations at varying layer depth. Across these three backbones, the mean Pearson correlation coefficient between the intrinsic dimension and validation accuracy is $\rho = 0.704$. The best performing layers exhibit the highest or second highest intrinsic dimension.

Benchmark Unless stated otherwise, we refer to our best-performing model with 14 layers of OpenCLIP ViT-H as TiViT. A full comparison of TiViT and TSFMs on the UCR and UEA test set is reported in Table 1. The state-of-the-art TSFM Mantis achieves a linear classification accuracy of 80.1% on the UCR benchmark. Our statistical analysis with a paired t-test and a significance level of 0.05 confirms that TiViT significantly outperforms ($p = 0.003$) Mantis across the 128 datasets of the UCR benchmark, achieving 81.6% accuracy. We further extend our analysis to multivariate time series. TiViT reaches a classification accuracy of 72.0%, which is statistically on par with Mantis on the UEA benchmark. The concatenation of per-channel representations, without learning any explicit cross-channel interactions, achieves state-of-the-art performance. In line with prior work (Feofanov et al., 2025), we could not observe any consistent benefit with channel-gating or attention pooling of channel-wise representations. Figure 5 shows that TiViT outperforms not only other TSFMs, but also a series of supervised learning (SL) and self-supervised learning (SSL) methods (pre-)trained per dataset. The comparison is limited to 91 UCR datasets since most of these models can only handle time series up to $T = 512$. Interestingly, TSFMs such as Chronos and VisionTS, primarily designed for forecasting, perform worse than TiViT or Mantis in time series classification. This highlights that models optimized for forecasting cannot be simply transferred to classification tasks and emphasizes the need for dedicated classification-focused TSFMs such as TiViT.

Table 2: Joint classification accuracy and alignment score for TiViTs and TSFMs on UCR.

Fusion	Model 1		Model 2		Joint accuracy	Alignment score
	Name	Acc	Name	Acc		
TSFM × TSFM	Mantis	80.1	Moment	79.0	81.5 (+1.4, +2.5)	0.222
TiViT × TiViT	CLIP	81.6	DINOv3	80.2	82.2 (+0.6, +2.0)	**0.431**
TiViT × TSFM	DINOv3	80.0	Moment	79.0	82.0 (+2.0, +3.0)	0.213
	DINOv3	80.0	Mantis	80.1	82.5 (+2.5, +2.4)	0.243
	CLIP	81.6	Moment	79.0	82.7 (+1.1, +3.7)	0.241
	CLIP	81.6	Mantis	80.1	**83.1** (+1.5, +3.0)	0.262

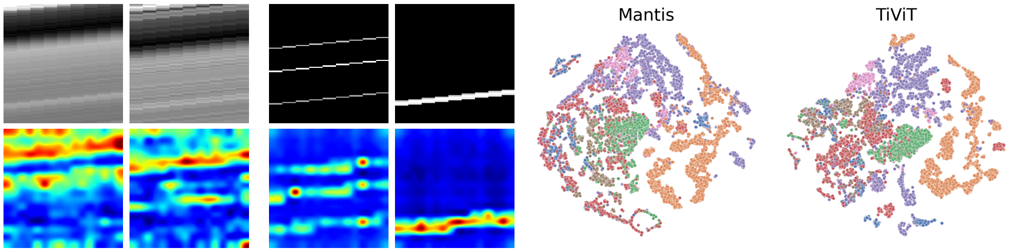

(a) Attention rollout

(b) t-SNE visualization

Figure 6: Qualitative analysis of TiViT representations on samples from the UCR benchmark.

4.3 ALIGNMENT AND FUSION OF TIVIT AND TSFM REPRESENTATIONS

We do not only compare the effectiveness of TiViT and TSFM representations against each other, but also explore their complementarity when concatenating their features for joint classification. As depicted in Table 2, the combination of TiViT and TSFM consistently improves the classification performance over any standalone model. While the combination of two TSFMs yields 81.5% accuracy, fusing TiViT-CLIP with Moment and Mantis leads to even higher accuracies of 82.7% and 83.1%, respectively. These results underscore the potential of multimodal time series analysis.

To uncover the differences between TiViTs and TSFMs, we assess the alignment of their representation spaces using the mutual k-nearest neighbor metric (Huh et al., 2024) on the 10 largest UCR datasets. Table 2 presents the average alignment scores across datasets for CLIP, DINOv3, Mantis, and Moment. Interestingly, the alignment score of the two TSFMs is relatively low. We hypothesize that this discrepancy arises from their different pretraining paradigms. A similarly low alignment score is observed between any TiViT and TSFM, which we attribute to their domain gap. TiViT and Mantis extract different representations for the same time series, which is beneficial for joint classification. The highest alignment is measured between TiViT-CLIP and TiViT-DINOv3, both of which are pretrained contrastively on image datasets.

4.4 FEATURE VISUALIZATION

To gain insights into the processing of TiViT, we employ attention rollout (Abnar & Zuidema, 2020) on images generated from the ECG200 and ElectricDevices datasets of the UCR archive. As shown in Figure 6a, the attention weights aggregated across layers highlight the most salient regions of the input. In particular, high attention weights align with the bright and dark areas in the 2D image representation, which correspond to high and low signals in the original time series. This indicates that TiViT attends to the critical signals necessary for distinguishing samples of different classes.

In addition, we compare the representations of TiViT and Mantis in Figure 6b using t-SNE (van der Maaten & Hinton, 2008) visualizations on the ElectricDevices dataset. Mantis is trained contrastively and can discover class-distinguishable time series representations without label supervision. Our findings go beyond this: even without any training on time series, TiViT generates embeddings that form clusters aligned with the ground-truth classes illustrated in different colors. More t-SNE visualizations for TiViT on UCR datasets are provided in Appendix D.11.

Table 3: Classification accuracy on UCR subsets (left) and comparison of classifiers (right).

Model	UCR subsets				Classification head		
	Small	Large	Short	Long	Logistic R.	Nearest C.	Random F.
Moment	86.6	85.4	87.4	67.3	79.0	68.4	75.7
Mantis	87.2	82.6	88.2	71.4	80.1	71.2	77.7
TiViT *(Ours)*	90.5	85.4	87.8	75.6	81.6	71.9	77.7
TiViT + Moment *(Ours)*	90.7	**87.2**	88.8	75.7	82.7	73.6	79.5
TiViT + Mantis *(Ours)*	**91.4**	86.2	**89.3**	**77.8**	**83.1**	**73.8**	**80.1**

Table 4: Anomaly detection on 248 datasets from the UCR Anomaly Archive. We compare the performance of TiViT to baselines reported by Goswami et al. (2024).

Metric		TiViT	MOMENT	GPT4TS	TimesNet	Anomaly TF	DGHL	k-NN
Adj. F1	Mean	**0.746** +0.118	0.628	0.424	0.537	0.492	0.425	0.554
	Median	**0.985** +0.207	0.778	0.331	0.541	0.432	0.331	0.595
	Std	0.368	0.373	0.366	0.389	0.401	0.365	0.393
VUS ROC	Mean	**0.770** +0.064	0.684	0.611	0.679	0.661	0.646	0.706
	Median	**0.795** +0.068	0.692	0.615	0.692	0.658	0.635	0.727
	Std	0.169	0.146	0.114	0.141	0.147	0.137	0.155

4.5 ABLATION STUDIES

In Section 4.2, we report the performance of TiViT across all 128 UCR datasets. To further explore its capabilities, we now select four UCR subsets: 10 datasets with the fewest training samples ($16 \leq N_{train} \leq 20$), the most training samples ($1000 \leq N_{train} \leq 8926$), the shortest time series ($15 \leq T \leq 80$), and the longest time series ($1500 \leq T \leq 2844$). The results are displayed in Table 3. TiViT significantly outperforms Mantis on subsets with a small training set (90.5% vs. 87.2%) and long time series (75.6% vs. 71.4%). These findings demonstrate that TiViT excels in generalizing from limited training data and in modeling long-range dependencies.

Finally, we investigate the effectiveness of TiViT in zero-shot classification with a nearest centroid classifier. On the UCR benchmark, TiViT achieves a zero-shot classification accuracy of 71.9%. Our approach surpasses both Mantis (71.2%) and Moment (68.4%), highlighting the ability of TiViT to extract generalizable representations. We further merge the representations of TiViT and Mantis, reaching a state-of-the-art zero-shot accuracy of 73.8%.

4.6 TASKS BEYOND CLASSIFICATION

As shown above, TiViT excels in time series classification, providing rich embeddings with a very strong zero-shot performance. This prompts us to apply it to anomaly detection, too, as both tasks are of a discriminative nature. To this end, Table 4 reports the performance of TiViT in time series anomaly detection following the setup considered in Goswami et al. (2024). We compare it to foundation models and specialized methods across 248 datasets from the UCR Anomaly Archive (Wu & Keogh, 2023) and observe that TiViT equipped with an OpenCLIP ViT-B backbone and a trainable linear reconstruction head achieves an adjusted best F1 score of 0.746, substantially outperforming Moment with a score of 0.628.

TiViT is especially tailored to discriminative tasks due to the large-scale contrastive pre-training of the ViT backbone. To verify the usefulness of TiViT in generative tasks, we provide preliminary results of its evaluation in long-term time series forecasting in Table 22 in the appendix. We note that TiViT reaches linear probing performance comparable to that of Moment on the 8 standard multivariate long-term forecasting datasets (Wu et al., 2021).

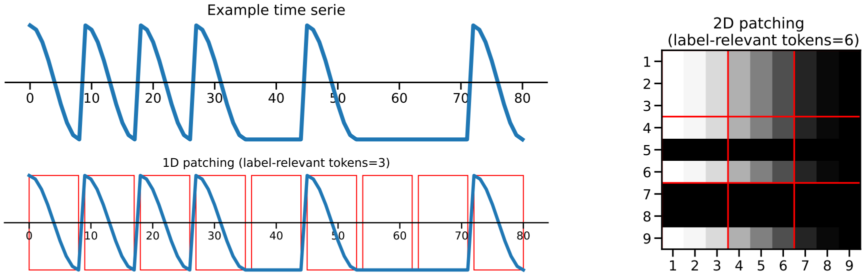

Figure 7: 2D patching yields a higher number of label-relevant tokens (with constant negative signal) than 1D patching. This facilitates time series classification with Transformers.

5 INSIGHTS ON MODELING TIME SERIES AS IMAGES

TiViT surpasses the performance of TSFMs in time series tasks by leveraging pretrained ViTs. This raises a key question: is its success solely due to the rich representations learned from billions of natural images, or is there an inherent advantage of the 2D patching strategy as well? We develop a theoretical insight at the patch level showing how the 2D representation of time series can enhance the classification performance of Transformer models. To empirically validate this, we compare the performance of Transformers pretrained on real-world data using 1D versus 2D patching.

5.1 THEORETICAL ANALYSIS OF 1D AND 2D PATCHING

We consider a binary time series classification problem with N univariate training samples $\{(\boldsymbol{t}^n, y^n), y^n \in \{+1, -1\}\}_{n=1}^N$. Each time series $\boldsymbol{t}^n \in \mathbb{R}^T$ can be patched as follows:

- 1D patching: The series $\boldsymbol{t}$ is split into k contiguous, non-overlapping tokens $\boldsymbol{x}_l \in \mathbb{R}^k$.
- 2D patching: The series $\boldsymbol{t}$ is reshaped into a $k \times k$ matrix, then divided into k non-overlapping $\sqrt{k} \times \sqrt{k}$ patches, which are flattened to form tokens $\boldsymbol{x}'_{(i,j)} \in \mathbb{R}^k$.

This setup ensures the same number of tokens for 1D and 2D patching. Our analysis builds on the notion of label-relevant tokens introduced by Li et al. (2023a). Following their data model, we consider each token to be a noisy version of distinct patterns. In binary classification, there exist two such patterns $\{\boldsymbol{\mu}_1, \boldsymbol{\mu}_2\}$, $\boldsymbol{\mu}_i \in \mathbb{R}^k, \forall\, i$. For a time series $\boldsymbol{t}^n$ with label $y^n = 1$, tokens $\boldsymbol{x}$ that are noisy $\boldsymbol{\mu}_1$, i.e., $||\boldsymbol{x} - \boldsymbol{\mu_1}|| \leq ||\boldsymbol{x} - \boldsymbol{\mu_2}||$, are label-relevant. Similarly, for a time series $\boldsymbol{t}^n$ with label $y^n = -1$, the noisy versions of $\boldsymbol{\mu}_2$ are label-relevant.

Benefits of 2D patching Li et al. (2023a) showed that the sample complexity of a Transformer scales as $\mathcal{O}(1/\alpha_*^2)$ where α_* denotes the fraction of label-relevant tokens in the training samples. In Appendix A.2, we provide a constructive proof showing that under certain conditions, this fraction of label-relevant tokens is greater when the time series is transformed into a 2D representation compared to the conventional 1D representation. Therefore, 2D patching can lead to more efficient learning with Transformers than 1D patching. Figure 7 illustrates our idea for an exemplary time series with $T = 91$ and $k = 9$. We set $\boldsymbol{\mu}_1 = \cos(x)$ for $x \in [0, \pi]$ and define the label-relevant signal as $\boldsymbol{\mu}_2 = -1$. In the 1D case, only three tokens carry the label-relevant information, whereas in the 2D case there are six such tokens. Following Li et al. (2023a), distributing the discriminative signal across a larger number of tokens makes it easier for a Transformer to detect and leverage it.

Interpretability scores To confirm our hypothesis about the spread of information achieved with 2D modeling, we now illustrate it on samples from a real-world dataset from the UCR repository. In particular, we show that a model trained on 2D representations of time series has more regions that it deems relevant for predicting the class membership of the time series. To this end, we follow Early et al. (2024) and use MILLET: a framework that provides interpretability scores for timestamps within a time series given a pretrained model. For this, we train two shallow ViTs, ViT1D and ViT2D, on the BirdChicken dataset from the UCR repository. ViT1D takes as input a raw 1D time series, while ViT2D is trained on square 2D images of the time series. The only difference between

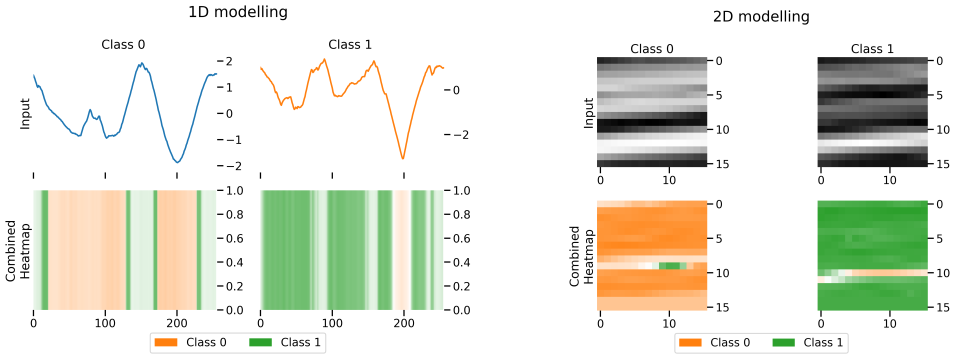

Figure 8: Comparison of interpretability heatmaps for two ViTs trained on 1D (left) and 2D (right) representations of time series from the BirdChicken dataset, respectively. The interpretability scores for the correct class of a sample are more homogeneous in the 2D case.

these two models is their patching strategy: ViT1D patches the time series using a 1D convolutional filter, while ViT2D applies a 2D convolutional filter. The obtained results for two samples from different classes are presented in Figure 8, for 1D (left) and 2D (right) cases, respectively. Note that the 1D heatmap for the sample with ground-truth class 0 highlights discriminative signals for class 1 at the beginning and end of the time series, while the corresponding 2D heatmap displays no such signals in these areas. The interpretability scores w.r.t. the ground-truth class of a sample are generally more homogeneous for ViT2D which facilitates classification.

5.2 PRETRAINING TRANSFORMERS WITH 1D AND 2D PATCHING

To validate our hypothesis about the benefits of 2D patching in practice, we study how patching affects the quality of representations learned by Transformers on real-world time series. In this experiment, we fix the Transformer architecture and pretraining method, and only vary the patching strategy. We then evaluate the representations learned by the model on the UCR benchmark. Following Feofanov et al. (2025), we pretrain a Transformer model with 6 layers and 8 heads per layer using contrastive learning. Details are provided in Appendix B. We compare 1D and 2D patching with both non-overlapping and overlapping patches. As summarized in Table 5, 2D patching outperforms 1D patching, with overlapping 2D patches yielding the highest classification accuracy. This finding shows that the transformation of time series to images is not only beneficial when leveraging pretrained ViTs, but can also enhance time series pretraining from scratch.

Table 5: Evaluation of models pretrained with different patching strategies on UCR.

Patching	Non-overlap		Overlap	
	1D	2D	1D	2D
Accuracy	76.4	76.8	76.6	**77.4**

6 CONCLUSION

In this paper, we introduced TiViT, the first method to successfully leverage large pretrained ViTs for time series classification. Our analysis revealed that the most effective features for this task are the hidden representations of ViTs which exhibit high intrinsic dimensionality. Building on this insight, TiViT significantly outperformed TSFMs in time series classification on the UCR benchmark and reached competitive results on UEA. We investigated the complementarity of TiViT and TSFMs, and by combining their representations, established the new state-of-the-art in zero-shot and linear classification on both benchmarks. Beyond the task of classification, TiViT excelled in time series anomaly detection on the UCR Anomaly Archive. We finally provided theoretical and empirical evidence that modeling time series in 2D rather than 1D is not only key to exploiting pretrained ViTs but broadly advantageous for time series pretraining and classification with Transformers.

Limitations and future work While our study evaluated time series representations via linear probing, future work could explore the finetuning of TiViT. Moreover, the powerful representations of large-scale ViTs present an opportunity for knowledge distillation into efficient time series models.

REFERENCES

Samira Abnar and Willem Zuidema. Quantifying attention flow in transformers. In *Proceedings of the 58th Annual Meeting of the Association for Computational Linguistics*, pp. 4190–4197, 2020.

Ralph G. Andrzejak, Klaus Lehnertz, Florian Mormann, Christoph Rieke, Peter David, and Christian E. Elger. Indications of nonlinear deterministic and finite-dimensional structures in time series of brain electrical activity: Dependence on recording region and brain state. *Physical Review E*, 64(6):061907, 2001.

Davide Anguita, Alessandro Ghio, Luca Oneto, Xavier Parra, and Jorge L. Reyes-Ortiz. A public domain dataset for human activity recognition using smartphones. In *21st European Symposium on Artificial Neural Networks, Computational Intelligence and Machine Learning*, pp. 437–442, 2013.

Abdul Fatir Ansari, Lorenzo Stella, Ali Caner Turkmen, Xiyuan Zhang, Pedro Mercado, Huibin Shen, Oleksandr Shchur, Syama Sundar Rangapuram, Sebastian Pineda Arango, Shubham Kapoor, Jasper Zschiegner, Danielle C. Maddix, Hao Wang, Michael W. Mahoney, Kari Torkkola, Andrew Gordon Wilson, Michael Bohlke-Schneider, and Bernie Wang. Chronos: Learning the language of time series. *Transactions on Machine Learning Research*, 2024.

Anthony Bagnall, Hoang Anh Dau, Jason Lines, Michael Flynn, James Large, Aaron Bostrom, Paul Southam, and Eamonn Keogh. The uea multivariate time series classification archive, 2018. *arXiv preprint arXiv:1811.00075*, 2018.

Sathya Kamesh Bhethanabhotla, Omar Swelam, Julien Siems, David Salinas, and Frank Hutter. Mamba4Cast: Efficient zero-shot time series forecasting with state space models. *arXiv preprint arXiv:2410.09385*, 2024.

Defu Cao, Furong Jia, Sercan O. Arik, Tomas Pfister, Yixiang Zheng, Wen Ye, and Yan Liu. TEMPO: Prompt-based generative pre-trained transformer for time series forecasting. In *The Twelfth International Conference on Learning Representations*, 2024.

Cristian I. Challu, Peihong Jiang, Ying Nian Wu, and Laurent Callot. Deep generative model with hierarchical latent factors for time series anomaly detection. In *Proceedings of The 25th International Conference on Artificial Intelligence and Statistics*, pp. 1643–1654, 2022.

Ching Chang, Wei-Yao Wang, Wen-Chih Peng, and Tien-Fu Chen. LLM4TS: Aligning pre-trained llms as data-efficient time-series forecasters. *ACM Transactions on Intelligent Systems and Technology*, 16(3), 2025.

Mouxiang Chen, Lefei Shen, Zhuo Li, Xiaoyun Joy Wang, Jianling Sun, and Chenghao Liu. VisionTS: Visual masked autoencoders are free-lunch zero-shot time series forecasters. *arXiv preprint arXiv:2408.17253*, 2024.

Mehdi Cherti, Romain Beaumont, Ross Wightman, Mitchell Wortsman, Gabriel Ilharco, Cade Gordon, Christoph Schuhmann, Ludwig Schmidt, and Jenia Jitsev. Reproducible scaling laws for contrastive language-image learning. In *Proceedings of the IEEE/CVF Conference on Computer Vision and Pattern Recognition*, pp. 2818–2829, 2023.

Gari D. Clifford, Chengyu Liu, Benjamin Moody, Li-wei H. Lehman, Ikaro Silva, Qiao Li, Alistair E. Johnson, and Roger G. Mark. AF classification from a short single lead ECG recording: The PhysioNet/computing in cardiology challenge 2017. In *2017 Computing in Cardiology (CinC)*, pp. 1–4, 2017.

Zhicheng Cui, Wenlin Chen, and Yixin Chen. Multi-scale convolutional neural networks for time series classification. *arXiv preprint arXiv:1603.06995*, 2016.

Abhimanyu Das, Weihao Kong, Rajat Sen, and Yichen Zhou. A decoder-only foundation model for time-series forecasting. In *Proceedings of the 41st International Conference on Machine Learning*, pp. 10148–10167, 2024.

Hoang Anh Dau, Anthony Bagnall, Kaveh Kamgar, Chin-Chia Michael Yeh, Yan Zhu, Shaghayegh Gharghabi, Chotirat Ann Ratanamahatana, and Eamonn Keogh. The ucr time series archive. *IEEE/CAA Journal of Automatica Sinica*, 6(6):1293–1305, 2019.

Jia Deng, Wei Dong, Richard Socher, Li-Jia Li, Kai Li, and Li Fei-Fei. ImageNet: A large-scale hierarchical image database. In *2009 IEEE Conference on Computer Vision and Pattern Recognition*, pp. 248–255, 2009.

Satvik Dixit, Laurie M. Heller, and Chris Donahue. Vision language models are few-shot audio spectrogram classifiers. In *NeurIPS Audio Imagination Workshop*, 2024.

Teresa Dorszewski, Lenka Tětková, Robert Jenssen, Lars Kai Hansen, and Kristoffer Knutsen Wickstrøm. From colors to classes: Emergence of concepts in vision transformers. *arXiv preprint arXiv:2503.24071*, 2025.

Alexey Dosovitskiy, Lucas Beyer, Alexander Kolesnikov, Dirk Weissenborn, Xiaohua Zhai, Thomas Unterthiner, Mostafa Dehghani, Matthias Minderer, Georg Heigold, Sylvain Gelly, Jakob Uszkoreit, and Neil Houlsby. An image is worth 16x16 words: Transformers for image recognition at scale. In *International Conference on Learning Representations*, 2021.

Joseph Early, Gavin Cheung, Kurt Cutajar, Hanting Xie, Jas Kandola, and Niall Twomey. Inherently interpretable time series classification via multiple instance learning. In *International Conference on Learning Representations*, 2024.

Emadeldeen Eldele, Mohamed Ragab, Zhenghua Chen, Min Wu, Chee Keong Kwoh, Xiaoli Li, and Cuntai Guan. Time-series representation learning via temporal and contextual contrasting. In *Proceedings of the Thirtieth International Joint Conference on Artificial Intelligence, IJCAI-21*, pp. 2352–2359, 2021.

Elena Facco, Maria d'Errico, Alex Rodriguez, and Alessandro Laio. Estimating the intrinsic dimension of datasets by a minimal neighborhood information. *Scientific Reports*, 7:12140, 2017.

Vasilii Feofanov, Songkang Wen, Marius Alonso, Romain Ilbert, Hongbo Guo, Malik Tiomoko, Lujia Pan, Jianfeng Zhang, and Ievgen Redko. Mantis: Lightweight calibrated foundation model for user-friendly time series classification. *arXiv preprint arXiv:2502.15637*, 2025.

Jean-Yves Franceschi, Aymeric Dieuleveut, and Martin Jaggi. Unsupervised scalable representation learning for multivariate time series. In H. Wallach, H. Larochelle, A. Beygelzimer, F. d'Alché-Buc, E. Fox, and R. Garnett (eds.), *Advances in Neural Information Processing Systems*, 2019.

Shanghua Gao, Teddy Koker, Owen Queen, Thomas Hartvigsen, Theodoros Tsiligkaridis, and Marinka Zitnik. UniTS: A unified multi-task time series model. In *Advances in Neural Information Processing Systems*, pp. 140589–140631, 2024.

Amin Ghiasi, Hamid Kazemi, Eitan Borgnia, Steven Reich, Manli Shu, Micah Goldblum, Andrew Gordon Wilson, and Tom Goldstein. What do vision transformers learn? a visual exploration. *arXiv preprint arXiv:2212.06727*, 2022.

Aldo Glielmo, Iuri Macocco, Diego Doimo, Matteo Carli, Claudio Zeni, Romina Wild, Maria d'Errico, Alex Rodriguez, and Alessandro Laio. DADApy: Distance-based analysis of data-manifolds in python. *Patterns*, 3(10):100589, 2022.

Ary L. Goldberger, Luis A. N. Amaral, Leon Glass, Jeffrey M. Hausdorff, Plamen Ch. Ivanov, Roger G. Mark, Joseph E. Mietus, George B. Moody, Chung-Kang Peng, and H. Eugene Stanley. PhysioBank, PhysioToolkit, and PhysioNet: components of a new research resource for complex physiologic signals. *Circulation*, 101(23):e215–e220, 2000.

Mononito Goswami, Cristian Ignacio Challu, Laurent Callot, Lenon Minorics, and Andrey Kan. Unsupervised model selection for time series anomaly detection. In *International Conference on Learning Representations*, 2023.

Mononito Goswami, Konrad Szafer, Arjun Choudhry, Yifu Cai, Shuo Li, and Artur Dubrawski. MOMENT: A family of open time-series foundation models. In *Proceedings of the 41st International Conference on Machine Learning*, pp. 16115–16152, 2024.

Nate Gruver, Marc Finzi, Shikai Qiu, and Andrew Gordon Wilson. Large language models are zero shot time series forecasters. In *Advances in Neural Information Processing Systems*, 2023.

Kaiming He, Haoqi Fan, Yuxin Wu, Saining Xie, and Ross Girshick. Momentum contrast for unsupervised visual representation learning. In *Proceedings of the IEEE/CVF Conference on Computer Vision and Pattern Recognition*, pp. 9729–9738, 2020.

Kaiming He, Xinlei Chen, Saining Xie, Yanghao Li, Piotr Dollár, and Ross Girshick. Masked autoencoders are scalable vision learners. In *Proceedings of the IEEE/CVF Conference on Computer Vision and Pattern Recognitio*, pp. 16000–16009, 2022.

Minyoung Huh, Brian Cheung, Tongzhou Wang, and Phillip Isola. Position: The platonic representation hypothesis. In *Proceedings of the 41st International Conference on Machine Learning*, pp. 20617–20642, 2024.

Romain Ilbert, Ambroise Odonnat, Vasilii Feofanov, Aladin Virmaux, Giuseppe Paolo, Themis Palpanas, and Ievgen Redko. Samformer: Unlocking the potential of transformers in time series forecasting with sharpness-aware minimization and channel-wise attention. In *Proceedings of the 41st International Conference on Machine Learning*, 2024.

Gabriel Ilharco, Mitchell Wortsman, Ross Wightman, Cade Gordon, Nicholas Carlini, Rohan Taori, Achal Dave, Vaishaal Shankar, Hongseok Namkoong, John Miller, Hannaneh Hajishirzi, Ali Farhadi, and Ludwig Schmidt. OpenCLIP, 2021. Version 0.1. URL: `https://doi.org/10.5281/zenodo.5143773`.

Ming Jin, Shiyu Wang, Lintao Ma, Zhixuan Chu, James Y Zhang, Xiaoming Shi, Pin-Yu Chen, Yuxuan Liang, Yuan-Fang Li, Shirui Pan, and Qingsong Wen. Time-LLM: Time series forecasting by reprogramming large language models. In *International Conference on Learning Representations*, 2024.

Bastiaan Kemp, Aeilko H. Zwinderman, Bert Tuk, Hilbert A. C. Kamphuisen, and Josefien J. L. Oberye. Analysis of a sleep-dependent neuronal feedback loop: the slow-wave microcontinuity of the EEG. *IEEE Transactions on Biomedical Engineering*, 47(9):1185–1194, 2000.

Christian Lessmeier, James K. Kimotho, Detmar Zimmer, and Walter Sextro. Condition monitoring of bearing damage in electromechanical drive systems by using motor current signals of electric motors: A benchmark data set for data-driven classification. *PHM Society European Conference*, 3(1), 2016.

Hongkang Li, Meng Wang, Sijia Liu, and Pin-Yu Chen. A theoretical understanding of shallow vision transformers: Learning, generalization, and sample complexity. In *International Conference on Learning Representations*, 2023a.

Zekun Li, Shiyang Li, and Xifeng Yan. Time series as images: Vision transformer for irregularly sampled time series. In *Advances in Neural Information Processing Systems*, pp. 49187–49204, 2023b.

Chenguo Lin, Xumeng Wen, Wei Cao, Congrui Huang, Jiang Bian, Stephen Lin, and Zhirong Wu. NuTime: Numerically multi-scaled embedding for large-scale time-series pretraining. *arXiv preprint arXiv:2310.07402*, 2023.

Jiayang Liu, Lin Zhong, Jehan Wickramasuriya, and Venu Vasudevan. uWave: Accelerometer-based personalized gesture recognition and its applications. In *2009 IEEE International Conference on Pervasive Computing and Communications*, 2009.

Xu Liu, Juncheng Liu, Gerald Woo, Taha Aksu, Yuxuan Liang, Roger Zimmermann, Chenghao Liu, Silvio Savarese, Caiming Xiong, and Doyen Sahoo. Moirai-MoE: Empowering time series foundation models with sparse mixture of experts. *arXiv preprint arXiv:2410.10469*, 2024a.

Yong Liu, Haoran Zhang, Chenyu Li, Xiangdong Huang, Jianmin Wang, and Mingsheng Long. Timer: Generative pre-trained transformers are large time series models. In *Proceedings of the 41st International Conference on Machine Learning*, pp. 32369–32399, 2024b.

Jingchao Ni, Ziming Zhao, ChengAo Shen, Hanghang Tong, Dongjin Song, Wei Cheng, Dongsheng Luo, and Haifeng Chen. Harnessing vision models for time series analysis: A survey. *arXiv preprint arXiv:2502.08869*, 2025.

Yuqi Nie, Nam H Nguyen, Phanwadee Sinthong, and Jayant Kalagnanam. A time series is worth 64 words: Long-term forecasting with transformers. In *International Conference on Learning Representations*, 2023.

Robert Thomas Olszewski. *Generalized feature extraction for structural pattern recognition in time-series data*. PhD thesis, Carnegie Mellon University, 2001.

Maxime Oquab, Timothée Darcet, Théo Moutakanni, Huy V. Vo, Marc Szafraniec, Vasil Khalidov, Pierre Fernandez, Daniel HAZIZA, Francisco Massa, Alaaeldin El-Nouby, Mido Assran, Nicolas Ballas, Wojciech Galuba, Russell Howes, Po-Yao Huang, Shang-Wen Li, Ishan Misra, Michael Rabbat, Vasu Sharma, Gabriel Synnaeve, Hu Xu, Herve Jegou, Julien Mairal, Patrick Labatut, Armand Joulin, and Piotr Bojanowski. DINOv2: Learning robust visual features without supervision. *Transactions on Machine Learning Research*, 2024.

Boris N. Oreshkin, Dmitri Carpov, Nicolas Chapados, and Yoshua Bengio. N-beats: Neural basis expansion analysis for interpretable time series forecasting. In *International Conference on Learning Representations*, 2020.

John Paparrizos, Paul Boniol, Themis Palpanas, Ruey S. Tsay, Aaron Elmore, and Michael J. Franklin. Volume under the surface: a new accuracy evaluation measure for time-series anomaly detection. *Proceedings of the VLDB Endowment*, 15(11):2774–2787, 2022.

Alec Radford, Jong Wook Kim, Chris Hallacy, Aditya Ramesh, Gabriel Goh, Sandhini Agarwal, Girish Sastry, Amanda Askell, Pamela Mishkin, Jack Clark, Gretchen Krueger, and Ilya Sutskever. Learning transferable visual models from natural language supervision. In *Proceedings of the 38th International Conference on Machine Learning*, pp. 8748–8763, 2021.

Sridhar Ramaswamy, Rajeev Rastogi, and Kyuseok Shim. Efficient algorithms for mining outliers from large data sets. *Proceedings of the 2000 ACM SIGMOD International Conference on Management of Data*, 29(2):427–438, 2000.

Kashif Rasul, Arjun Ashok, Andrew Robert Williams, Hena Ghonia, Rishika Bhagwatkar, Arian Khorasani, Mohammad Javad Darvishi Bayazi, George Adamopoulos, Roland Riachi, Nadhir Hassen, Marin Biloš, Sahil Garg, Anderson Schneider, Nicolas Chapados, Alexandre Drouin, Valentina Zantedeschi, Yuriy Nevmyvaka, and Irina Rish. Lag-Llama: Towards foundation models for probabilistic time series forecasting. *arXiv preprint arXiv:2310.08278*, 2024.

Christoph Schuhmann, Romain Beaumont, Richard Vencu, Cade W Gordon, Ross Wightman, Mehdi Cherti, Theo Coombes, Aarush Katta, Clayton Mullis, Mitchell Wortsman, Patrick Schramowski, Srivatsa R Kundurthy, Katherine Crowson, Ludwig Schmidt, Robert Kaczmarczyk, and Jenia Jitsev. LAION-5B: An open large-scale dataset for training next generation image-text models. *Advances in Neural Information Processing Systems*, pp. 25278–25294, 2022.

Joan Serrà, Santiago Pascual, and Alexandros Karatzoglou. Towards a universal neural network encoder for time series. In *International Conference of the Catalan Association for Artificial Intelligence*, 2018.

Oriane Siméoni, Huy V. Vo, Maximilian Seitzer, Federico Baldassarre, Maxime Oquab, Cijo Jose, Vasil Khalidov, Marc Szafraniec, Seungeun Yi, Michaël Ramamonjisoa, Francisco Massa, Daniel Haziza, Luca Wehrstedt, Jianyuan Wang, Timothée Darcet, Théo Moutakanni, Leonel Sentana, Claire Roberts, Andrea Vedaldi, Jamie Tolan, John Brandt, Camille Couprie, Julien Mairal, Hervé Jégou, Patrick Labatut, and Piotr Bojanowski. Dinov3. *arXiv preprint arXiv:2508.10104*, 2025.

Pattreeya Tanisaro and Gunther Heidemann. Time series classification using time warping invariant echo state networks. In *IEEE International Conference on Machine Learning and Applications (ICMLA)*, pp. 831–836, 2016.

Sana Tonekaboni, Danny Eytan, and Anna Goldenberg. Unsupervised representation learning for time series with temporal neighborhood coding. In *International Conference on Learning Representations*, 2021.

Michael Tschannen, Alexey Gritsenko, Xiao Wang, Muhammad Ferjad Naeem, Ibrahim Alabdulmohsin, Nikhil Parthasarathy, Talfan Evans, Lucas Beyer, Ye Xia, Basil Mustafa, Olivier Hénaff, Jeremiah Harmsen, Andreas Steiner, and Xiaohua Zhai. SigLIP 2: Multilingual vision-language encoders with improved semantic understanding, localization, and dense features. *arXiv preprint arXiv:2502.14786*, 2025.

Lucrezia Valeriani, Diego Doimo, Francesca Cuturello, Alessandro Laio, Alessio Ansuini, and Alberto Cazzaniga. The geometry of hidden representations of large transformer models. In *Advances in Neural Information Processing Systems*, pp. 51234–51252, 2023.

Laurens van der Maaten and Geoffrey Hinton. Visualizing data using t-sne. *Journal of Machine Learning Research*, 9(86):2579–2605, 2008. URL `http://jmlr.org/papers/v9/vandermaaten08a.html`.

Ashish Vaswani, Noam Shazeer, Niki Parmar, Jakob Uszkoreit, Llion Jones, Aidan N Gomez, Łukasz Kaiser, and Illia Polosukhin. Attention is all you need. *Advances in Neural Information Processing Systems*, pp. 5998–6008, 2017.

Yihang Wang, Yuying Qiu, Peng Chen, Kai Zhao, Yang Shu, Zhongwen Rao, Lujia Pan, Bin Yang, and Chenjuan Guo. ROSE: Register assisted general time series forecasting with decomposed frequency learning. *arXiv preprint arXiv:2405.17478*, 2024.

Zhiguang Wang, Weizhong Yan, and Tim Oates. Time series classification from scratch with deep neural networks: A strong baseline. In *International Joint Conference on Neural Networks (IJCNN)*, pp. 1578–1585, 2017.

Haixu Wu, Jiehui Xu, Jianmin Wang, and Mingsheng Long. Autoformer: Decomposition transformers with auto-correlation for long-term series forecasting. In *Advances in Neural Information Processing Systems*, 2021.

Haixu Wu, Tengge Hu, Yong Liu, Hang Zhou, Jianmin Wang, and Mingsheng Long. TimesNet: Temporal 2d-variation modeling for general time series analysis. In *International Conference on Learning Representations*, 2023.

Renjie Wu and Eamonn J. Keogh. Current time series anomaly detection benchmarks are flawed and are creating the illusion of progress. *IEEE Transactions on Knowledge and Data Engineering*, 35 (3):2421–2429, 2023.

Zhifeng Xie, Shengye Yu, Qile He, and Mengtian Li. SonicVisionLM: Playing sound with vision language models. In *Proceedings of the IEEE/CVF Conference on Computer Vision and Pattern Recognition*, pp. 26866–26875, 2024.

Jiehui Xu, Haixu Wu, Jianmin Wang, and Mingsheng Long. Anomaly transformer: Time series anomaly detection with association discrepancy. In *International Conference on Learning Representations*, 2022.

Hao Xue and Flora D. Salim. PromptCast: A new prompt-based learning paradigm for time series forecasting. *IEEE Transactions on Knowledge and Data Engineering*, 36(11):6851–6864, 2024.

Zhihan Yue, Yujing Wang, Juanyong Duan, Tianmeng Yang, Congrui Huang, Yunhai Tong, and Bixiong Xu. Ts2vec: Towards universal representation of time series. *Proceedings of the AAAI Conference on Artificial Intelligence*, 36(8):8980–8987, 2022.

Mariusz Zebik, Marcin Korytkowski, Rafal Angryk, and Rafał Scherer. Convolutional neural networks for time series classification. In *Artificial Intelligence and Soft Computing*, pp. 635–642. Springer International Publishing, 2017.

Ailing Zeng, Muxi Chen, Lei Zhang, and Qiang Xu. Are transformers effective for time series forecasting? In *Proceedings of the AAAI Conference on Artificial Intelligence*, volume 37, pp. 11121–11128, 2023.

George Zerveas, Srideepika Jayaraman, Dhaval Patel, Anuradha Bhamidipaty, and Carsten Eickhoff. A transformer-based framework for multivariate time series representation learning. In *Proceedings of the 27th ACM SIGKDD Conference on Knowledge Discovery & Data Mining*, pp. 2114–2124, 2021.

Xiaohua Zhai, Basil Mustafa, Alexander Kolesnikov, and Lucas Beyer. Sigmoid loss for language image pre-training. In *2023 IEEE/CVF International Conference on Computer Vision*, pp. 11941–11952, 2023.

Kai Zhang, Rong Zhou, Eashan Adhikarla, Zhiling Yan, Yixin Liu, Jun Yu, Zhengliang Liu, Xun Chen, Brian D. Davison, Hui Ren, Jing Huang, Chen Chen, Yuyin Zhou, Sunyang Fu, Wei Liu, Tianming Liu, Xiang Li, Yong Chen, Lifang He, James Zou, Quanzheng Li, Hongfang Liu, and Lichao Sun. A generalist vision–language foundation model for diverse biomedical tasks. *Nature Medicine*, pp. 3129–3141, 2024.

Tian Zhou, Ziqing Ma, Qingsong Wen, Xue Wang, Liang Sun, and Rong Jin. FEDformer: Frequency enhanced decomposed transformer for long-term series forecasting. In *Proceedings of the 39th International Conference on Machine Learning*, pp. 27268–27286, 2022.

Tian Zhou, Peisong Niu, Liang Sun, and Rong Jin. One fits all: Power general time series analysis by pretrained lm. In *Advances in Neural Information Processing Systems*, volume 36, pp. 43322–43355, 2023.

A DETAILS ON THE THEORETICAL ANALYSIS

We first review the shallow ViT and data model introduced by Li et al. (2023a) in their theoretical analysis of training a ViT. Their Theorem A.1 shows that the sample complexity for ViTs to achieve a zero generalization error is inversely correlated with the fraction of label-relevant tokens. Building on this insight, we introduce and proof Proposition 1, showing that 2D patching can increase the number of label-relevant tokens compared to 1D patching. We further illustrate our Proposition 1 with various examples of time series and their corresponding 2D representations.

A.1 BACKGROUND

Model and setup Following the setup of Li et al. (2023a), we study a binary classification problem with N training samples $\{(\boldsymbol{X}^n, y^n)\}_{n=1}^N$. Each input $\boldsymbol{X}^n \in \mathbb{R}^{d\times L}$ contains L tokens $\{\boldsymbol{x}_1^n, \ldots, \boldsymbol{x}_L^n\}$. Labels $y^n \in \{\pm 1\}$ are determined by majority vote over discriminative tokens. A simplified Vision Transformer (ViT) (Dosovitskiy et al., 2021) model is defined as:

$$F(\boldsymbol{X}^n) = \frac{1}{|\mathcal{S}^n|}\sum_{l\in\mathcal{S}^n} \boldsymbol{a}_{(l)}^\top \text{ReLU}\left(\boldsymbol{W}_O\boldsymbol{W}_V\boldsymbol{X}^n \text{softmax}\left({\boldsymbol{X}^n}^\top \boldsymbol{W}_K^\top \boldsymbol{W}_Q \boldsymbol{x}_l^n\right)\right),$$

where $\psi = (\boldsymbol{A} = \{\boldsymbol{a}_{(l)}\}_l, \boldsymbol{W}_O, \boldsymbol{W}_V, \boldsymbol{W}_K, \boldsymbol{W}_Q)$ are trainable parameters. The empirical risk minimization problem is:

$$\min_{\psi} f_N(\psi) = \frac{1}{N}\sum_{n=1}^{N} \max\left\{1 - y^n \cdot F(\boldsymbol{X}^n), 0\right\}.$$

Training uses mini-batch SGD with fixed output layer weights $\boldsymbol{A}$, following standard NTK initialization practices.

Data model Tokens $\boldsymbol{x}_l^n$ are noisy versions of M patterns $\{\boldsymbol{\mu}_1, \ldots, \boldsymbol{\mu}_M\}$, where $\boldsymbol{\mu}_1, \boldsymbol{\mu}_2$ are discriminative. Label y^n depends on majority vote over tokens closest to $\boldsymbol{\mu}_1/\boldsymbol{\mu}_2$. Noise level τ satisfies $\tau < \kappa/4$, with $\kappa - 4\tau = \Theta(1)$.

Generalization of ViT We now recap the main results from Li et al. (2023a) from which we derive our result, along with the main notations in Table 6.

Assumption (Initial Model Conditions, Li et al. (2023a)). *Initial weights* $\boldsymbol{W}_V^{(0)}, \boldsymbol{W}_K^{(0)}, \boldsymbol{W}_Q^{(0)}$ *satisfy:*

$$\|\boldsymbol{W}_V^{(0)}\boldsymbol{\mu}_j - \boldsymbol{p}_j\| \le \sigma, \quad \|\boldsymbol{W}_K^{(0)}\boldsymbol{\mu}_j - \boldsymbol{q}_j\| \le \delta, \quad \|\boldsymbol{W}_Q^{(0)}\boldsymbol{\mu}_j - \boldsymbol{r}_j\| \le \delta,$$

for orthonormal bases $\mathcal{P}, \mathcal{Q}, \mathcal{R}$ *and* $\sigma = O(1/M), \delta < 1/2$.

Theorem (Generalization of ViT, Li et al. (2023a)). *Under Assumption 1, with sufficient model width* $m \gtrsim \epsilon^{-2}M^2\log N$, *fraction*

$$\alpha_* \ge \alpha_\#/(\epsilon_S e^{-(\delta+\tau)}(1-(\sigma+\tau)),$$

and sample size

$$N \ge \Omega\left((\alpha_* - c'(1-\zeta) - c''(\sigma+\tau))^{-2}\right),$$

SGD achieves zero generalization error after

$$T = \Theta\left(\frac{1}{(1-\epsilon-(\sigma+\tau)M/\pi)\eta\alpha_*}\right)$$

iterations.

Proposition (Generalization without Self-Attention, Li et al. (2023a)). *Without self-attention, achieving zero error requires* $N \ge \Omega\left((\alpha_*(\alpha_* - \sigma - \tau))^{-2}\right)$, *demonstrating ViT's sample complexity reduction by* $1/\alpha_*^2$.

Table 6: Key Notations

Notation	Description
α_*	Fraction of label-relevant tokens
σ, δ, τ	Initialization/token noise parameters
κ	Minimum pattern distance
M	Total number of patterns

A.2 PROOF OF LABEL RELEVANCE IN 2D PATCHES

We introduce Proposition 1 that formalizes our theoretical analysis of 1D and 2D patching from Section 5.1 and provide a detailed proof.

Proposition 1. *For an arbitrary $\boldsymbol{\mu}_1, \boldsymbol{\mu}_2 \in \mathbb{R}^k$, let $\boldsymbol{t} = [\boldsymbol{x}_1 \ \boldsymbol{x}_2 \ \cdots \ \boldsymbol{x}_k]^\top \in \mathbb{R}^T$ where $\forall i \in [k], \boldsymbol{x}_i \in \mathbb{R}^k$ and either $\boldsymbol{x}_i = \boldsymbol{\mu}_1$ or $\boldsymbol{x}_i = \boldsymbol{\mu}_2$ with $\boldsymbol{\mu}_2$ being a label-relevant pattern. Let $|\{i : \boldsymbol{x}_i = \boldsymbol{\mu}_2\}| = n'$ and assume that $2\boldsymbol{x}' \cdot (\boldsymbol{\mu}_1 - \boldsymbol{\mu}_2) \leq ||\boldsymbol{\mu}_1||^2 - ||\boldsymbol{\mu}_2||^2$ whenever $|\{i : x'_i \in \boldsymbol{\mu}_2\}| \geq \sqrt{k}$. Then, it holds that*

$$\alpha_*^{2D} \geq \alpha_*^{1D} = \frac{n'}{k},$$

and the inequality is strict if n' mod $\sqrt{k} > 0$.

Proof. For a token $\boldsymbol{x}'^n$ to be label-relevant (aligned with $\boldsymbol{\mu}_2$), it must satisfy:

$$\|\boldsymbol{x}'^n - \boldsymbol{\mu}_2\| \leq \|\boldsymbol{x}'^n - \boldsymbol{\mu}_1\|.$$

Expanding both sides, we have that:

$$\|\boldsymbol{x}'^n\|^2 + 2\boldsymbol{x}'^n \cdot \boldsymbol{\mu}_1 + \|\boldsymbol{\mu}_1\|^2 \leq \|\boldsymbol{x}'^n\|^2 - 2\boldsymbol{x}'^n \cdot \boldsymbol{\mu}_2 + \|\boldsymbol{\mu}_2\|^2.$$

Regrouping the terms gives us the desired condition:

$$2\boldsymbol{x}'^n \cdot (\boldsymbol{\mu}_1 - \boldsymbol{\mu}_2) \leq ||\boldsymbol{\mu}_1||^2 - ||\boldsymbol{\mu}_2||^2. \tag{1}$$

Recall that n' denotes the number of segments of $\boldsymbol{\mu}_2$ in time series $\boldsymbol{t}$. Each such segment spans $\sqrt{k}$ tokens, contributing at least $\sqrt{k}$ elements to each of them. Under the assumption of the proposition, it implies (1) and makes each of these $\sqrt{k}$ tokens label-relevant.

We now need to carefully consider how the $\boldsymbol{\mu}_2$ segments can be placed within $\boldsymbol{t}$ to understand how many tokens become label-relevant thanks to each $\boldsymbol{\mu}_2$. We consider two cases: 1) $n' = c\sqrt{k}$ for some $c \in \mathbb{N}$ satisfying $n' \in (0, k]$, and 2) $n' = c\sqrt{k} + b$ for some $a, b \in \mathbb{N}$, $\sqrt{k} > b > 0$ such that $n' \in (0, k]$. In the first case, $\alpha_*^{\text{1D}} = c\sqrt{k}/k$. In the case of 2D patching, in the worst case, $\boldsymbol{\mu}_2$ segments can be placed such that they will contribute to $c\sqrt{k}$ tokens. In this case, $\alpha_*^{\text{2D}} \geq c\sqrt{k}/k$ and $\alpha_*^{\text{1D}} \leq \alpha_*^{\text{2D}}$. If n' is not a multiple of $\sqrt{k}$, the same analysis applies for the $c\sqrt{k}$ segments of $\boldsymbol{\mu}_2$. To account for the remainder b, we note that for any $b > 0$, in 2D case, it adds $\sqrt{k}$ label-relevant tokens to the fraction α_*^{2D} so that $\alpha_*^{\text{2D}} \geq \frac{c\sqrt{k}+\sqrt{k}}{k}$. In the case of 1D patching, $\alpha_*^{\text{1D}} = \frac{c\sqrt{k}+b}{k}$. Given that $b < \sqrt{k}$, this concludes the proof. ☐

A.3 ADDITIONAL ILLUSTRATIONS OF PROPOSITION 1

To illustrate the benefits of 2D modeling and patching, we present several examples of time series in Figure 9. We define $\boldsymbol{\mu}_1$ using functions such as log, cosine, and sine. We then set $\boldsymbol{\mu}_2 = \mathbf{1}_k$, $n' = 3$ and randomly shuffle $\boldsymbol{\mu}_1$ and $\boldsymbol{\mu}_2$ segments within the generated input time series.

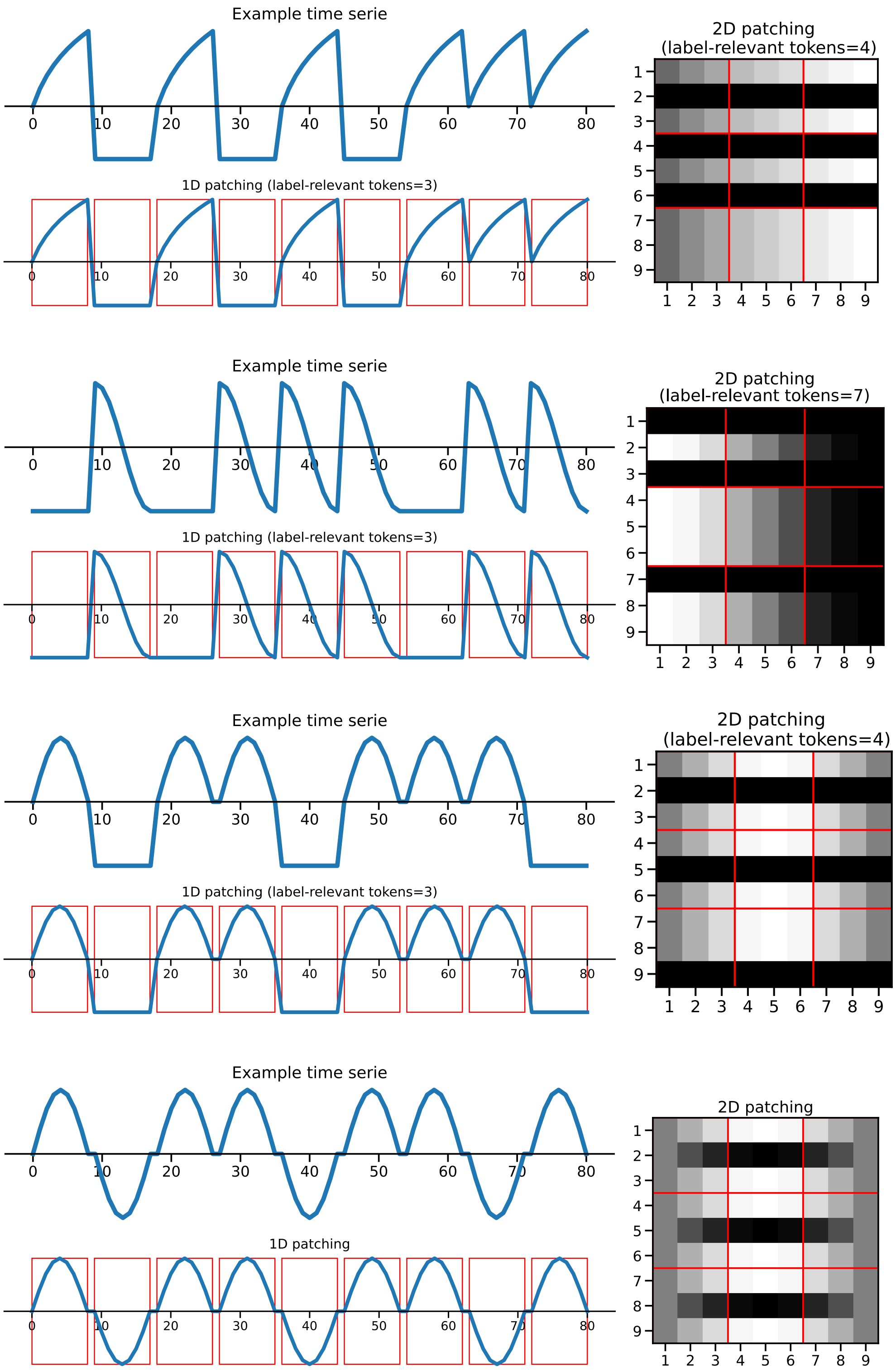

Figure 9: Illustration of Proposition 1 on more generated time series. In each example considered, 2D patching is more beneficial due the higher number of label-relevant tokens.

Table 7: Data used to pretrain Transformers for comparison of 1D and 2D patching.

Dataset	Number of examples	Prop. of taken examples
ECG	20835	45.7%
EMG	163	100%
Epilepsy	11480	100%
FD-A	10912	100%
FD-B	13619	100%
Gesture	1320	100%
HAR	20835	78.7%
SleepEEG	20836	4.5%

B DETAILS ON THE COMPARISON OF 1D AND 2D PATCHING FOR TRANSFORMERS

B.1 ARCHITECTURE AND PRETRAINING

To evaluate the effect of 1D versus 2D patching on representations learned by Transformers, we fix the Transformer architecture and pretraining strategy, and only change the patching approach for generating input tokens. We adopt the setup of Feofanov et al. (2025) since their Transformer block implementation (ViTUnit class here) for time series classification is similar to the classical ViT. Specifically, the model comprises 6 Transformer layers, each with 8 attention heads and an embedding dimension of 256.

For pretraining, we employ contrastive learning following (Feofanov et al., 2025; He et al., 2020). The augmentation technique to generate positive pairs is RandomCropResize with a crop rate varying within $[0\%, 20\%]$. All time series are resized to a fixed length $T = 512$ using interpolation.

We examine both non-overlapping and overlapping patches following Goswami et al. (2024); Nie et al. (2023). For non-overlapping 1D patching, we generate 32 patches of size 16. For non-overlapping 2D patching, we first arrange the 1D patches in a matrix of size 32×16 and then extract 32 patches of size 2×8. After flattening, we obtain 32 patches of size 16, similar to the 1D setting, but semantically different. For overlapping 1D patching, we apply a stride of 8, which yields 64 patches of size 16. For overlapping 2D patching, we rearrange these 1D patches again in a matrix of size 64×16 and then extract 32 patches of size 4×8. Flattening yields 32 patches of size 32.

B.2 DATASET

To pretrain the different models, we first generate a pretraining dataset from publicly available datasets that are not part of the evaluation benchmark. In detail, we consider a concatenation of the following datasets: ECG (Clifford et al., 2017), EMG (Goldberger et al., 2000), Epilepsy (Andrzejak et al., 2001), FD-A and FD-B (Lessmeier et al., 2016), Gesture (Liu et al., 2009), HAR (Anguita et al., 2013), SleepEEG (Kemp et al., 2000). To reduce computation time, we construct a subset of the full dataset containing 100 000 samples, with a sufficiently balanced distribution across the individual source datasets. We give more details in Table 7 on how many samples were taken from each dataset to form the pretraining corpus.

C DETAILS ON THE EXPERIMENTAL SETUP

Datasets UCR (Dau et al., 2019) comprises 128 univariate time series datasets of varying sample size ($16 \leq N_{\text{train}} \leq 8926$) and series length ($15 \leq T \leq 2844$). UEA (Bagnall et al., 2018) consists of 30 multivariate time series datasets. Following Feofanov et al. (2025), we exclude three datasets (AtrialFibrillation, StandWalkJump, PenDigits) from UEA in our main evaluation due to their short sequence length or small test size.

Vision Transformers Our study mainly examines three differently pretrained ViTs: OpenCLIP (Cherti et al., 2023; Ilharco et al., 2021), SigLIP 2 (Tschannen et al., 2025), and DINOv3 (Siméoni et al., 2025). CLIP (Radford et al., 2021) performs contrastive learning of image and text encoders on image-text pairs. We reuse the ViT image encoders of OpenCLIP (Cherti et al., 2023; Ilharco et al., 2021) models trained with the LAION-2B English subset of LAION-5B (Schuhmann et al., 2022). SigLIP 2 (Tschannen et al., 2025) adopts contrastive learning on image-text pairs, but with a Sigmoid loss, complemented by captioning-based pretraining, self-distillation, and masked prediction. In contrast, DINOv3 (Siméoni et al., 2025) is solely pretrained on images through self-distillation with a student-teacher architecture and objectives at both the image and patch level. For each pretraining approach, we consider multiple vision model sizes (ViT-B, ViT-L, ViT-H) with varying layer depth (12, 24, and 32 layers). Additionally, we investigate the effectiveness of ViTs from DINOv2 (Oquab et al., 2024) and Masked Autoencoders (He et al., 2022) in the appendix.

Baselines We compare TiViT to two state-of-the-art TSFMs exclusively pretrained on time series. Mantis (Feofanov et al., 2025) is a Transformer model (8 M parameters) comprising 6 layers and 8 heads per layer, pretrained on 2 million time series with contrastive learning. As stated by Feofanov et al. (2025), Mantis is based on the ViT architecture, making it particularly suitable for our comparison with large-scale ViTs trained on natural images. Moment (Goswami et al., 2024) is a family of Transformers pretrained on 13 million time series with masked modeling. In our study, we consider Moment-base with 12 layers and 125 M parameters.

We further consider GPT4TS (Zhou et al., 2023) pretrained on textual data and a wide range of supervised and self-supervised baselines (pre-)trained per time series dataset. The 9 supervised baselines comprise: ResNet (Wang et al., 2017), FCN (Wang et al., 2017), DTW (Dau et al., 2019), CNN (Zebik et al., 2017), MLP (Wang et al., 2017), Encoder (Serrà et al., 2018), TWIESN (Tanisaro & Heidemann, 2016), MCNN (Cui et al., 2016), and TimesNet (Wu et al., 2023). The 5 self-supervised baselines are: TS2Vec (Yue et al., 2022), T-Loss (Franceschi et al., 2019), TS-TCC (Eldele et al., 2021), TNC (Tonekaboni et al., 2021), and TST (Zerveas et al., 2021). For all of these baselines, we utilize the classification accuracy reported by Goswami et al. (2024) in our comparison.

Furthermore, we evaluate the effectiveness of two state-of-the-art TSFMs that have been designed for time series forecasting in time series classification: Chronos Bolt Base (Ansari et al., 2024) and VisionTS (Chen et al., 2024) with MAE Base backbone. We average the sequence of their output representations to obtain a single representation for linear classification.

Implementation To assess the effectiveness of TiViT and TSFM representations in time series classification, we train a logistic regressor with the LBFGS solver per dataset. Our evaluation adheres to the standard train-test splits provided by the UCR and UEA archive and reserves 20% of the train split for validation. For the time series-to-image transformation, we resize the grayscale images to the resolution expected by the ViT with nearest interpolation and adjust the contrast with a factor of 0.8. To compute the mutual kNN alignment score between models, we select the 10 largest UCR datasets, sample 1024 time series from each dataset, and measure the overlap of their representations for k=5. This setup is in line with Huh et al. (2024). All experiments can be performed on a single NVIDIA V100 GPU with 16 GB memory.

Anomaly detection For this task, we equip TiViT with 6 layers of OpenCLIP ViT-B, apply no patch overlap, and flatten the sequence of representations before learning a linear reconstruction head per dataset. TiViT is evaluated across 248 dataset from the UCR Anomaly Archive (Wu & Keogh, 2023) and compared to the following baselines: Moment (Goswami et al., 2024), GPT4TS (Zhou et al., 2023), TimesNet (Wu et al., 2023), Anomaly Transformer (Xu et al., 2022), DGHL (Challu et al., 2022), and kNN (Ramaswamy et al., 2000) with $k = 5$. We utilize the adjusted best F1 score (Goswami et al., 2023; Challu et al., 2022) and VUS-ROC score (Paparrizos et al., 2022) reported for each baseline by Goswami et al. (2024).

Forecasting We further evaluate TiViT in long-horizon time series forecasting on 8 standard datasets (Wu et al., 2021; Ilbert et al., 2024). Similar to the best setup for anomaly detection, TiViT utilizes 6 layers of OpenCLIP ViT-B as backbone, applies no patch overlap, and flattens the sequence of representations. A linear forecasting head is learned per dataset and forecasting horizon in $\{96, 192, 336, 720\}$. Our comparison considers 8 baselines. There are 2 TSFMs evaluated with linear probing: Moment (Goswami et al., 2024) and GPT4TS (Zhou et al., 2023). Moreover, there are 6 supervised methods: PatchTST (Nie et al., 2023), DLinear (Zeng et al., 2023), TimesNet (Wu et al., 2023), FEDformer (Zhou et al., 2022), N-BEATS (Oreshkin et al., 2020), and Stationary. The

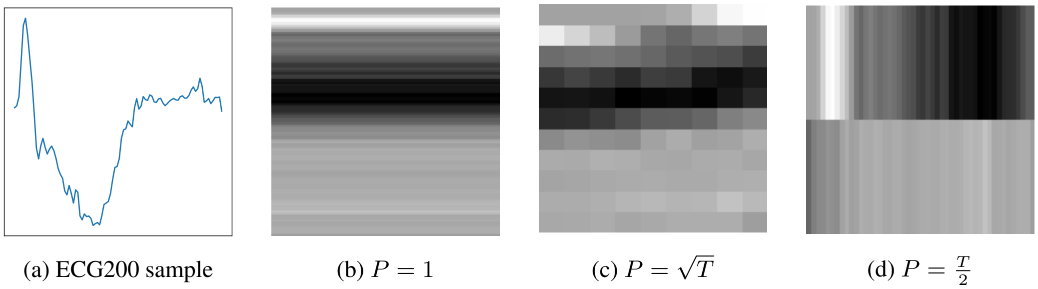
(a) ECG200 sample (b) $P = 1$ (c) $P = \sqrt{T}$ (d) $P = \frac{T}{2}$

Figure 10: Effect of patch size P on the time series-to-image transformation of a sample from the ECG 200 (Olszewski, 2001) dataset. To match the ViT input resolution, a small patch size ($P = 1$) requires horizontal stretching, while a large patch size ($P = \frac{T}{2}$) requires vertical stretching. Both scenarios result in redundant tokens.

Table 8: Effect of patch size and overlap on validation accuracy on UCR benchmark.

Patch size	$\sqrt{T}$			P^*		
Overlap	0.0	0.5	0.9	0.0	0.5	0.9
Val accuracy	78.0	80.3	80.7	88.1	88.9	89.7
Test accuracy	78.3	80.4	81.6	79.3	80.7	81.7

Mean Squared Error (MSE) and Mean Absolute Error (MAE) per baseline have been reported by Goswami et al. (2024).

D ADDITIONAL ANALYSIS ON TIVIT

D.1 PATCH SIZE AND OVERLAP

In Section 4.1, we report for TiViT that a patch size $P = \sqrt{T}$ and a stride $S = \frac{P}{10}$ yields high classification accuracy on any time series of length T. The patch size parameter P affects the visual appearance of the image representation provided to the ViT for feature extraction. Figure 10 displays a time series sample from the ECG200 Olszewski (2001) dataset along with its corresponding image representations for three different patch sizes. After patching and stacking, the 2D matrix is resized to the quadratic image resolution required by ViTs. Using very small (Figure 10b) or very large (Figure 10d) patch sizes results in redundant tokens representing the same input signal. To avoid a computationally expensive hyperparameter search to find the best patch size P^* per dataset, we propose to select $P = \sqrt{T}$ for any dataset of length T. A patch size of $\sqrt{T}$ yields a square-shaped image prior to resizing and thus the most diverse set of patches without any horizontal or vertical distortion (Figure 10c). Moreover, this setting is in line with our theoretical consideration in Section 5.1.

Table 8 presents the classification accuracy for TiViT with a CLIP backbone (TiViT-CLIP) and both non-overlapping and overlapping patches. To provide an upper bound on the classification performance, we perform a hyperparameter search for the best patch size P^*. Specifically, for each dataset of length T, we consider 20 equally spaced values in $[1, \frac{T}{2}]$ and identify the patch size that maximizes classification accuracy on the validation set. Note that, while there is a small decline in accuracy in the case of no overlap, when consistently applying $P = \sqrt{T}$, the computational cost is reduced by a factor of 20. The impact of the correct patch size vanishes with increasing overlap. Figure 11 visualizes the effect of patch overlap for TiViT with CLIP, DINOv2, and SigLIP 2 backbones while fixing the patch size at $P = \sqrt{T}$. All versions of TiViT achieve high classification accuracy when utilizing an overlap of 0.9 (corresponding to stride $S = \frac{P}{10}$).

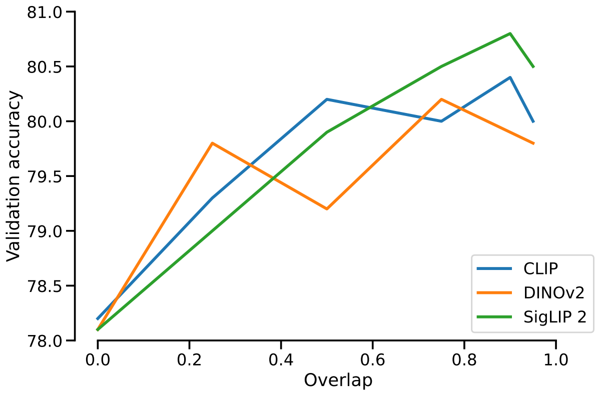

Figure 11: Effect of patch overlap on the classification accuracy of TiViT with different backbones.

Table 9: Comparison of interpolation methods on the UCR benchmark.

Interpolation	Antialias	Accuracy
Bilinear	False	81.2
	True	80.9
Bicubic	False	79.1
	True	79.1
Lanczos	-	80.6
Nearest	-	81.6

D.2 INTERPOLATION ALGORITHM FOR IMAGE RESIZING

In our time series-to-image transformation, we resize the grayscale images to the resolution expected by the ViT with nearest interpolation by default. To further investigate the impact of the resizing method, we conduct additional experiments using bilinear and bicubic interpolation, both with and without antialiasing, and Lanczos interpolation. Table 9 summarizes our results on the UCR benchmark and indicates that nearest interpolation yields the highest classification accuracy. We hypothesize that nearest interpolation is optimal for TiViT since it preserves the raw time series signals without introducing any smoothing artifacts.

D.3 IMAGING METHOD FOR TIME SERIES

In Section 3, we describe the transformation of time series into grayscale heatmaps, motivated by our theoretical insight in Section 5.1. Here, we explore two alternative image representations. Specifically, we visualize the time series as line plots, similar to Li et al. (2023b), and Gramian Angular Fields (GAF). We provide these 2D representations to TiViT and evaluate their effectiveness for classification on the UCR benchmark. For the two new imaging methods, we perform a hyperparameter search on the hidden layers ([10, 14, 18]) and choose the best configuration based on validation accuracy. The test accuracy is shown in Table 10. Our results indicate that TiViT achieves the highest classification accuracy using the heatmap-based representations.

D.4 AGGREGATION OF HIDDEN TOKEN REPRESENTATIONS

As described in Section 3, we obtain a single embedding for each time series by averaging the ViT hidden representations in a particular layer. We now evaluate the performance of TiViT when using the CLS token from each layer instead. Table 11 compares the linear classification performance on the UCR dataset using either the CLS token or the mean of all tokens. To ensure a fair comparison, we determine the best performing layer for each approach based on the validation accuracy. Across

Table 10: Comparison of imaging methods on the UCR benchmark.

Imaging method	Backbone	Layer	Accuracy
Gramian Angular Field	ViT-H/14	14	76.4
Lineplot	ViT-H/14	14	80.7
Heatmap	ViT-H/14	14	81.6

Table 11: Linear classification accuracy of TiViT on the UCR dataset with different ways of aggregating the hidden representations per layer. We report the total number of layers including the output layer and the index of the best performing layer starting from 0.

Model	# Layers	Average of tokens		CLS token	
		Layer	Accuracy	Layer	Accuracy
TiViT-DINOv2	25	15	80.0	17	79.1
TiViT-SigLIP 2	28	10	80.6	14	71.7
TiViT-CLIP	33	14	**81.6**	18	78.6

all backbones, the CLS token consistently results in lower test accuracy, confirming our choice to use the mean hidden representation in TiViT. Interestingly, the best performing CLS tokens appear in later layers compared to the best performing mean tokens. Therefore, utilizing the mean representations does not only enhance classification accuracy, but also reduce computational cost.

D.5 INTRINSIC DIMENSION AND PRINCIPAL COMPONENTS OF HIDDEN REPRESENTATIONS

The intrinsic dimension quantifies the minimum number of variables required to represent a local neighborhood of samples in the representation space. To estimate the intrinsic dimension, the TWO-NN estimator introduced by Facco et al. (2017) leverages the distance of each data point to its first and second nearest neighbor. As noted by the authors, a larger number of data points reduces the average distance to the second neighbor, and thus increases the intrinsic dimension. To mitigate this effect, they propose to subsample the dataset. Given a dataset of size N, we report the intrinsic dimension for $\frac{N}{4}$ subsamples in the main paper, which is in line with Valeriani et al. (2023). In Figure 12, we compare the intrinsic dimension of average representations from hidden layers using N, $\frac{N}{2}$, $\frac{N}{4}$, and $\frac{N}{8}$ samples for estimation. The layer with the highest intrinsic dimension, which is central to our analysis, remains the same regardless of the subsampling ratio.

Since the intrinsic dimension only characterizes the local geometry of the representation space, we further provide a global analysis using principal components. Specifically, in Figure 13, we determine the number of principal components that are necessary to cover 95% of the variance in the data. For DINOv2, we observe a peak in the number of principal components in the middle layers that corresponds to the layers achieving the best classification accuracy. Interestingly, CLIP

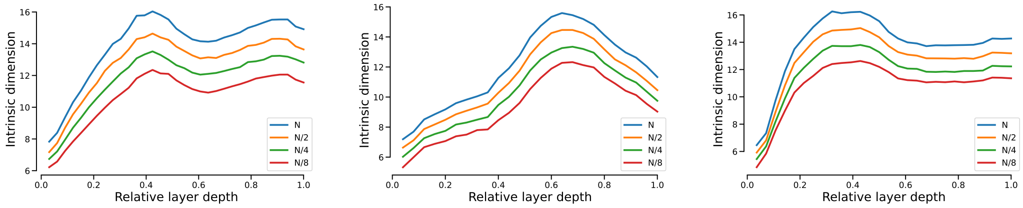

(a) TiViT-CLIP (b) TiViT-DINOv2 (c) TiViT-SigLIP 2

Figure 12: Intrinsic dimension of hidden representations per layer from CLIP, DINOv2, and SigLIP computed for subsamples of the dataset in $\{N, \frac{N}{2}, \frac{N}{4}, \frac{N}{8}\}$.

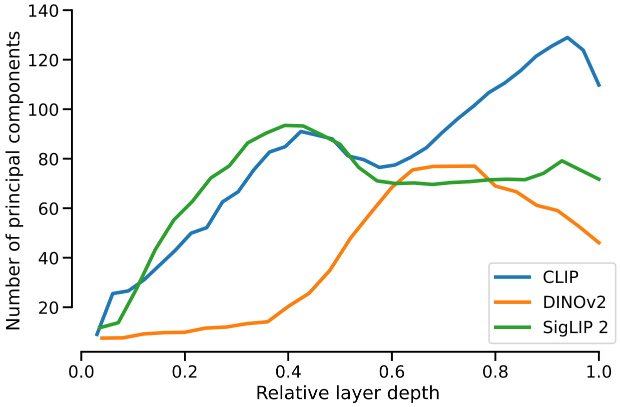

Figure 13: Number of principal components necessary to cover 95% of variance in the ViT representations per layer averaged across UCR datasets.

Table 12: Linear classification with TiViT on the UCR benchmark. For each model, we report the test accuracy achieved with the best performing hidden layer.

Model	Architecture	Layer (Max)	Parameters	Data	Accuracy
TiViT-DINOv3	ViT-L/14	17 (25)	202 M	LVD-1689M	80.2
TiViT-SigLIP 2	SoViT-400m/14	12 (28)	184 M	WebLI (10B)	80.6
TiViT-CLIP	ViT-H/14	14 (33)	257 M	LAION-2B	**81.6**

and SigLIP 2 exhibit two peaks in the number of principal components across the layers. The middle-layers corresponding to the first peak yield the highest time series classification accuracy.

D.6 SIZE OF VIT BACKBONE

We report the performance of TiViT with CLIP ViT-H backbone in Section 4.2 of the main paper. Table 13 provides a detailed analysis of how the performance of TiViT varies with the size of the ViT backbone, including ViT-B (with two patch sizes), ViT-L, and ViT-H. Remarkably, with only 6 Transformer layers from ViT-B, TiViT achieves an accuracy of 80.8%. While matching the number of Transformer layers in Mantis, TiViT surpasses Mantis (80.1%) in classification accuracy. However, the hidden dimensionality is higher for the ViT-B backbone used in TiViT. By utilizing a larger backbone, specifically 14 hidden layers of ViT-H/14, we achieve the highest accuracy of 81.3%, significantly outperforming conventional TSFMs.

D.7 SIZE OF PRETRAINING DATASET

ViTs are pretrained on massive image datasets to learn rich and transferable features. These image datasets are orders of magnitude larger than the time series corpora used to pretrain models such as Mantis (2M samples) or Moment (13M samples). To investigate how the size of the ViT pretraining

Table 13: Linear classification of TiViT-CLIP with varying size of the ViT backbone. For each model, we report the test accuracy on the UCR dataset achieved with the best performing hidden layer representation and the number of parameters up to this layer.

Architecture	Layer (total number)	Parameters	Accuracy
ViT-B/32	8 (13)	52 M	79.8
ViT-B/16	6 (13)	36 M	80.8
ViT-L/14	10 (25)	178 M	80.3
ViT-H/14	14 (33)	257 M	**81.6**

Table 14: Comparison of CLIP-ViT-L-14 pretraining datasets on UCR benchmark.

Dataset	Backbone	Layer	Accuracy
Laion400M	CLIP-ViT-L/14	10	81.6
Laion2B	CLIP-ViT-L/14	10	80.5

Table 15: Comparison of different backbones and feature extraction layers on the UCR benchmark.

Backbone	Layer	Accuracy
ViT-H/14	14	81.6
ConvNeXt-XXLarge	15	82.1

dataset affects the classification performance of TiViT, we compare TiViT with a CLIP-ViT-L backbone pretrained on 400M and 2B samples. As shown in Table 14, the model pretrained on 400M images outperforms the one pretrained on 2B images in time series classification. This suggests that dataset size alone does not guarantee superior performance in cross-domain tasks.

D.8 CONVOLUTIONAL BACKBONE

We focus our study on ViTs because they are the most widely used vision backbones, trained on the largest datasets, and thus enable a comparison of different pretraining paradigms. Nonetheless, we also include a comparison with CNN-based methods. DINOv2, SigLIP 2, and MAE are exclusively built upon ViTs, and thus the only setting we can identify with a convolutional backbone (ConvNeXt) is OpenCLIP. We perform an ablation study for TiViT using different ConvNeXt layers in $\{10, 15, 20, 25\}$ and evaluate the classification accuracy on the UCR benchmark. As shown in Table 15, our method TiViT is fully compatible with pretrained convolutional models and can achieve even higher accuracies on the UCR benchmark when using a ConvNeXt backbone compared to the typical ViT.

D.9 MASKED AUTOENCODER BACKBONE

In the main paper, we analyze the reusability of ViT backbones from CLIP Radford et al. (2021); Schuhmann et al. (2022), DINOv3 Siméoni et al. (2025), and SigLIP 2 Tschannen et al. (2025) in time series classification. In contrast, Chen et al. (2024) repurpose Masked Autoencoders (MAEs) He et al. (2022) for time series forecasting. To enable a direct comparison, we now utilize the hidden representations of MAE Base, Large, and Huge in time series classification.

Our analysis in Table 16 shows that for MAEs using the CLS token yields better performance in time series classification than averaging token representations. Moreover, Table 16 presents a comparison across MAEs of different sizes, showing that larger backbones consistently achieve higher accuracy. Different from contrastively pretrained models, summarized in Table 12 of the main paper, the best representations for time series classification with MAE lie in later layers. We further observe that the hidden representations of the later MAE layers up to the output layer perform similar in time series classification, while there is a significant gap between hidden representations and output

Table 16: Linear classification accuracy of TiViT with varying MAE backbone size and aggregation of hidden representations per layer. We report the total number of layers including the output layer and the index of the best performing layer starting from 0.

Architecture	# Layers	Average of tokens		CLS token	
		Layer	Acc	Layer	Acc
MAE Base	13	8	72.7	9	73.8
MAE Large	25	14	74.3	18	75.6
MAE Huge	33	20	75.9	20	**76.7**

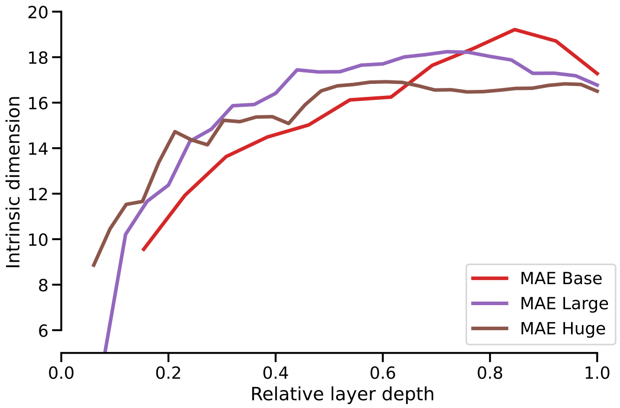

Figure 14: Intrinsic dimensionality of CLS tokens per MAE layer averaged across UCR datasets.

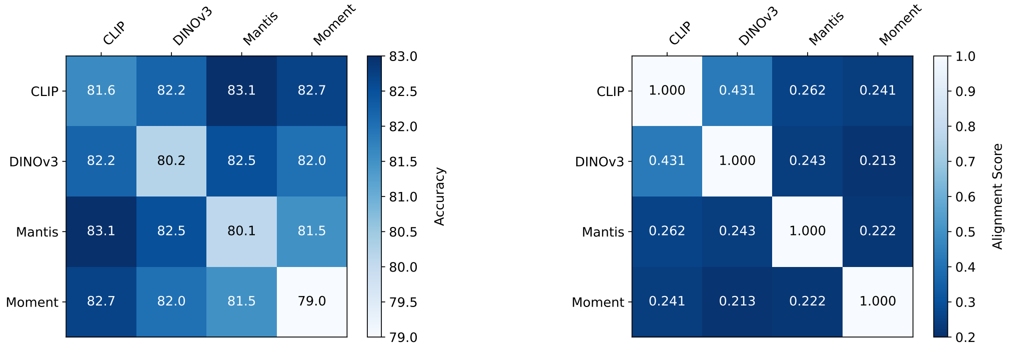

(a) Pairwise joint classification accuracy.

(b) Pairwise alignment score (mutual kNN).

Figure 15: The representations of frozen ViTs and TSFMs are concatenated and used in linear classification. Results are averaged over 128 datasets from the UCR benchmark.

representations for TiViT-CLIP (see Figure 4a in the main paper). Figure 14 illustrates the intrinsic dimension of the CLS tokens per layer averaged across the UCR datasets. We observe that the intrinsic dimension increases up to 60% of the layer depth, while the later layers mostly exhibit a similar intrinsic dimension, explaining their similar classification performance.

It is worth noting that MAE has only been pretrained on ImageNet-1k Deng et al. (2009) with 1.5 million samples, whereas CLIP has been pretrained on the significantly larger LAION-2B Schuhmann et al. (2022) dataset with 2 billion samples. We hypothesize that being exposed to a larger set of images during training enhances the capacity of a vision model to extract discriminative patterns from 2D time series representations.

D.10 ALIGNMENT AND FUSION OF TIVIT AND TSFM REPRESENTATIONS

In Table 2 of our main paper, we report the alignment and joint classification accuracy for TiViT and TSFMs. Figure 15 is an additional visualization of the pairwise scores as heatmaps.

D.11 FEATURE VISUALIZATION

In Section 4.4, we apply attention rollout to two samples from the ECG200 dataset, demonstrating that TiViT attends to salient regions of the time series images. Figure 17 further illustrates this behavior with three examples each from the AllGestureWiimoteX and ElectricDevices datasets, showing the original image, the corresponding attention rollout, and the overlay.

We further employ t-SNE to investigate the structure of the representations extracted by TiViT. Figure 16 presents t-SNE visualizations for 12 additional datasets. The results underscore TiViT's ability to uncover intrinsic cluster structures without access to labels and without being explicitly trained on time series.

Another way of understanding the features learned by ViTs is noise maximization. Ghiasi et al. (2022) have generated images that highly activate a particular feature in ViTs starting from random noise. TiViT applies a frozen backbone and thus utilizes the exact same features of a ViT learned from natural images. Their visualizations underline that ViT-B captures general edges and textures in early layers, and more specialized objects in later layers. Please note that TiViT only uses the first six layers of ViT-B, where there are mostly patterns and less semantic components.

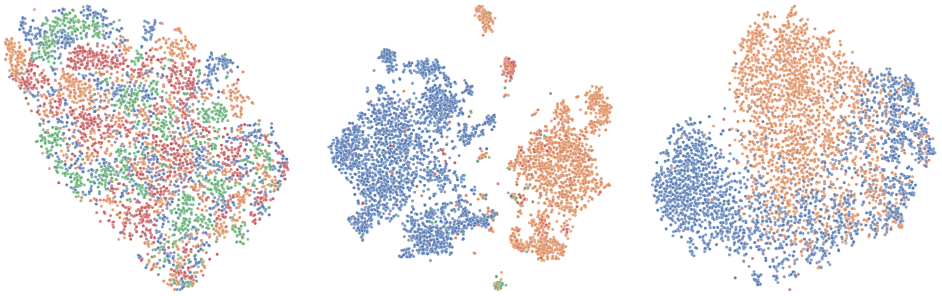

(a) TwoPatterns (b) ECG5000 (c) FordA

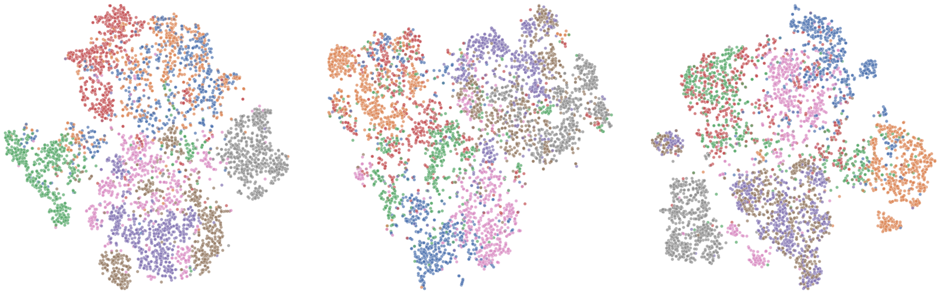

(d) UWaveGestureLibraryX (e) UWaveGestureLibraryY (f) UWaveGestureLibraryZ

(g) UWaveGestureLibraryAll (h) FordB (i) ChlorineConcentration

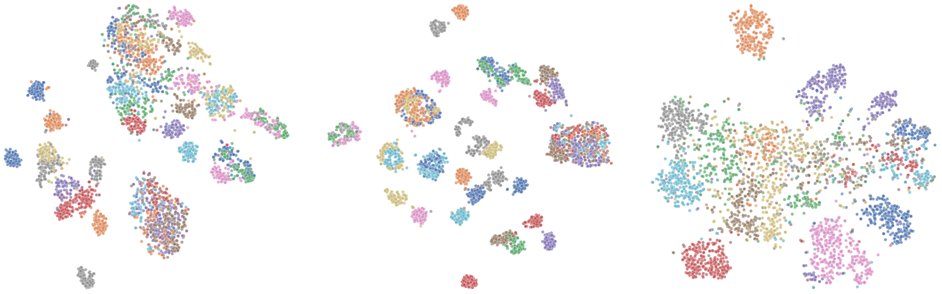

(j) NonInvasiveFetalECG1 (k) NonInvasiveFetalECG2 (l) MelbournePedestrian

Figure 16: t-SNE visualizations

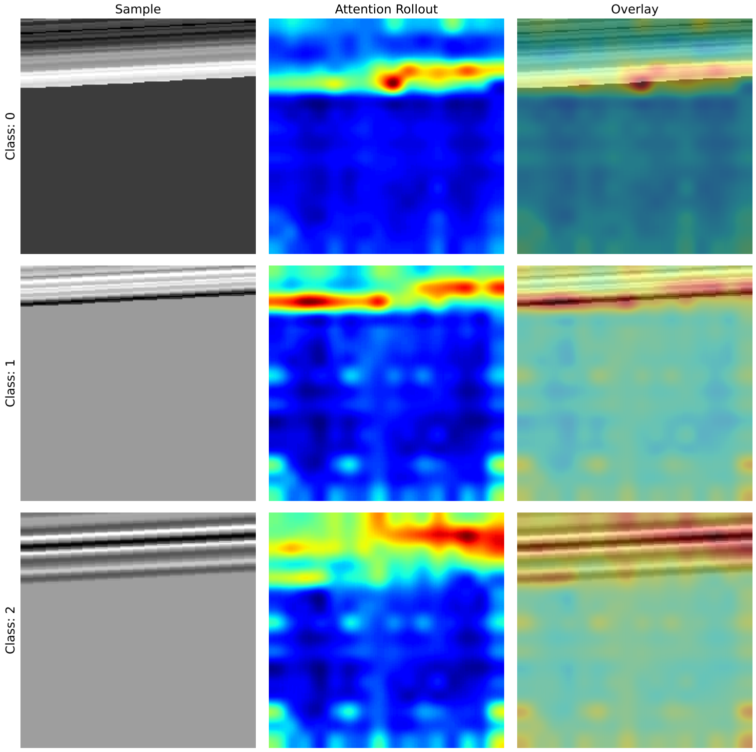

(a) AllGestureWiimoteX

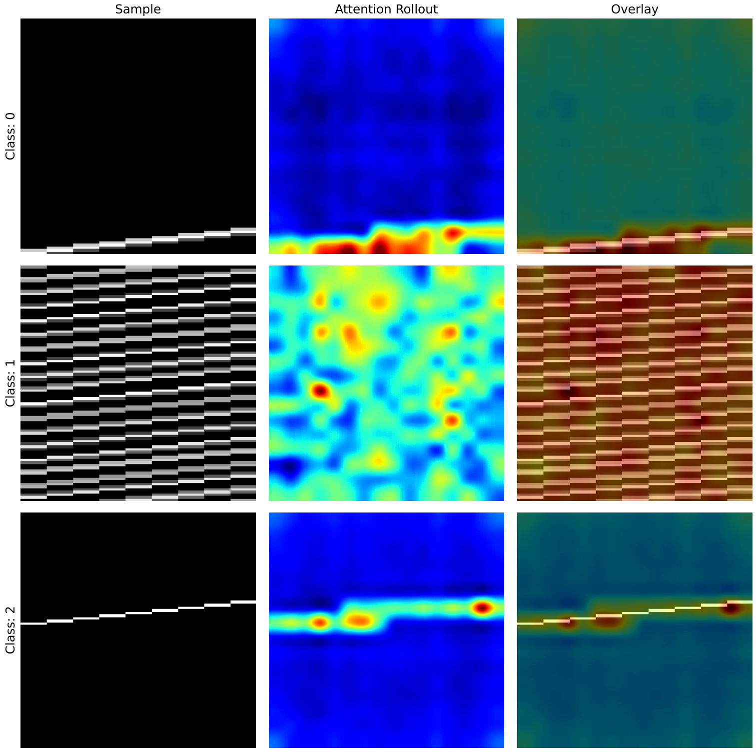

(b) ElectricDevices

Figure 17: Attention rollout.

E DETAILED BENCHMARKING RESULTS

In the main paper, we report the average accuracy of TiViT and TSFM across 128 univariate datasets from the UCR archive and 27 multivariate datasets from the UEA archive. Here, we report the full linear classification benchmark with accuracy scores for Mantis, Moment, TiViT, and their combinations on each dataset. Table 17 presents the performance on the UCR dataset, while Table 18 reports the results on the UEA dataset. Additionally, Table 19 provides the mean rank of all five methods on both benchmarks. If multiple element share the same rank, we assign them the lowest rank in the group. Comparisons with supervised and self-supervised baselines are provided in Table 20 for the UCR benchmark and in Table 21 for the UEA benchmark.

Furthermore, we assess the performance of TiViT against baseline methods in time series forecasting on 8 standard datasets (Table 22) and in time series anomaly detection on 248 datasets from the UCR Anomaly Archive (Table 23).

Table 17: Classification accuracy for 128 univariate datasets from the UCR benchmark. We report the mean and standard deviation across three random seeds.

Dataset	Moment	Mantis	TiViT	TiViT + Moment	TiViT + Mantis
ACSF1	0.673 ± 0.012	0.667 ± 0.021	**0.773** ± 0.015	**0.773** ± 0.006	0.757 ± 0.015
Adiac	0.728 ± 0.004	0.728 ± 0.011	0.708 ± 0.009	**0.732** ± 0.008	0.730 ± 0.012
AllGestureWiimoteX	0.686 ± 0.010	0.699 ± 0.003	0.685 ± 0.010	0.717 ± 0.009	**0.726** ± 0.001
AllGestureWiimoteY	0.710 ± 0.006	0.742 ± 0.007	0.721 ± 0.015	0.750 ± 0.022	**0.760** ± 0.014
AllGestureWiimoteZ	0.605 ± 0.007	0.673 ± 0.018	0.658 ± 0.015	0.690 ± 0.014	**0.700** ± 0.014
ArrowHead	0.804 ± 0.012	0.745 ± 0.007	0.819 ± 0.049	**0.851** ± 0.015	0.829 ± 0.035
BME	0.936 ± 0.010	0.991 ± 0.010	0.991 ± 0.015	0.987 ± 0.018	**0.996** ± 0.008
Beef	0.667 ± 0.067	0.689 ± 0.019	**0.800** ± 0.067	**0.800** ± 0.000	0.789 ± 0.069
BeetleFly	0.850 ± 0.050	0.867 ± 0.058	0.917 ± 0.058	0.917 ± 0.058	**0.950** ± 0.000
BirdChicken	0.883 ± 0.029	**0.950** ± 0.000	0.917 ± 0.029	0.900 ± 0.000	0.933 ± 0.029
CBF	0.907 ± 0.030	0.990 ± 0.009	**0.999** ± 0.001	0.997 ± 0.004	**0.999** ± 0.001
Car	0.856 ± 0.035	0.828 ± 0.010	0.844 ± 0.010	0.878 ± 0.010	**0.889** ± 0.025
Chinatown	0.962 ± 0.003	**0.964** ± 0.006	0.950 ± 0.018	0.954 ± 0.025	**0.964** ± 0.010
ChlorineConcentration	0.733 ± 0.010	0.643 ± 0.009	0.728 ± 0.008	**0.744** ± 0.012	0.738 ± 0.000
CinCECGTorso	0.719 ± 0.056	0.727 ± 0.021	**0.868** ± 0.034	0.837 ± 0.063	0.860 ± 0.039
Coffee	**1.000** ± 0.000	**1.000** ± 0.000	**1.000** ± 0.000	**1.000** ± 0.000	**1.000** ± 0.000
Computers	0.712 ± 0.036	0.740 ± 0.012	**0.785** ± 0.005	0.784 ± 0.011	0.781 ± 0.023
CricketX	0.706 ± 0.020	0.726 ± 0.015	0.753 ± 0.006	0.757 ± 0.013	**0.765** ± 0.011
CricketY	0.693 ± 0.018	0.732 ± 0.017	0.765 ± 0.006	0.776 ± 0.008	**0.783** ± 0.012
CricketZ	0.740 ± 0.016	0.721 ± 0.009	0.773 ± 0.017	0.779 ± 0.006	**0.791** ± 0.012
Crop	0.709 ± 0.003	0.695 ± 0.001	0.675 ± 0.001	**0.714** ± 0.003	0.707 ± 0.002
DiatomSizeReduction	0.900 ± 0.030	0.881 ± 0.032	**0.949** ± 0.055	0.935 ± 0.048	0.944 ± 0.054
DistalPhalanxOutlineAgeGroup	0.743 ± 0.011	**0.746** ± 0.017	0.703 ± 0.015	0.729 ± 0.011	0.717 ± 0.011
DistalPhalanxOutlineCorrect	0.762 ± 0.017	0.728 ± 0.007	**0.769** ± 0.029	0.766 ± 0.008	0.757 ± 0.014
DistalPhalanxTW	0.643 ± 0.004	**0.698** ± 0.007	0.640 ± 0.012	0.671 ± 0.011	0.626 ± 0.019
DodgerLoopDay	0.442 ± 0.014	**0.517** ± 0.036	0.488 ± 0.043	0.467 ± 0.014	0.508 ± 0.040
DodgerLoopGame	0.691 ± 0.062	0.720 ± 0.018	0.797 ± 0.045	0.766 ± 0.073	**0.802** ± 0.061
DodgerLoopWeekend	**0.986** ± 0.013	0.978 ± 0.007	0.959 ± 0.011	0.981 ± 0.008	0.969 ± 0.015
ECG200	0.843 ± 0.006	0.840 ± 0.017	**0.863** ± 0.006	0.847 ± 0.031	0.847 ± 0.021
ECG5000	0.934 ± 0.002	0.926 ± 0.005	0.934 ± 0.002	**0.936** ± 0.003	**0.936** ± 0.004
ECGFiveDays	0.919 ± 0.059	0.967 ± 0.012	0.953 ± 0.030	**0.972** ± 0.032	0.959 ± 0.028
EOGHorizontalSignal	0.559 ± 0.012	0.542 ± 0.014	0.598 ± 0.008	0.634 ± 0.008	**0.642** ± 0.012
EOGVerticalSignal	0.462 ± 0.021	**0.530** ± 0.013	0.445 ± 0.006	0.476 ± 0.016	0.471 ± 0.008
Earthquakes	**0.734** ± 0.025	0.707 ± 0.018	0.698 ± 0.007	0.717 ± 0.008	0.703 ± 0.017
ElectricDevices	0.626 ± 0.006	0.698 ± 0.003	**0.757** ± 0.009	0.741 ± 0.003	0.748 ± 0.007
EthanolLevel	**0.649** ± 0.008	0.433 ± 0.004	0.574 ± 0.008	0.617 ± 0.013	0.586 ± 0.008
FaceAll	0.724 ± 0.006	**0.797** ± 0.007	0.741 ± 0.005	0.743 ± 0.005	0.762 ± 0.007
FaceFour	0.826 ± 0.076	**0.958** ± 0.007	0.871 ± 0.029	0.909 ± 0.034	0.936 ± 0.035
FacesUCR	0.789 ± 0.010	0.888 ± 0.003	0.881 ± 0.007	0.881 ± 0.004	**0.912** ± 0.004
FiftyWords	0.733 ± 0.015	0.736 ± 0.010	0.758 ± 0.013	0.788 ± 0.003	**0.796** ± 0.006
Fish	0.949 ± 0.000	0.954 ± 0.000	0.952 ± 0.007	0.945 ± 0.020	**0.968** ± 0.013
FordA	0.915 ± 0.002	0.910 ± 0.003	0.915 ± 0.003	**0.927** ± 0.004	0.917 ± 0.000
FordB	0.801 ± 0.004	0.769 ± 0.002	**0.812** ± 0.005	0.809 ± 0.007	0.800 ± 0.012
FreezerRegularTrain	0.973 ± 0.011	0.976 ± 0.012	**0.997** ± 0.002	0.996 ± 0.005	**0.997** ± 0.002
FreezerSmallTrain	0.840 ± 0.012	0.870 ± 0.020	**0.992** ± 0.004	0.982 ± 0.006	0.990 ± 0.003
Fungi	0.753 ± 0.033	0.810 ± 0.025	0.787 ± 0.022	0.806 ± 0.014	**0.812** ± 0.023
GestureMidAirD1	0.659 ± 0.012	0.664 ± 0.027	0.746 ± 0.013	0.731 ± 0.023	**0.756** ± 0.032
GestureMidAirD2	0.567 ± 0.016	0.585 ± 0.040	0.667 ± 0.012	0.644 ± 0.032	**0.669** ± 0.015
GestureMidAirD3	0.359 ± 0.019	0.392 ± 0.013	**0.472** ± 0.016	0.449 ± 0.016	0.464 ± 0.025
GesturePebbleZ1	0.893 ± 0.015	0.917 ± 0.003	0.895 ± 0.006	0.924 ± 0.000	**0.928** ± 0.003
GesturePebbleZ2	0.846 ± 0.018	**0.895** ± 0.007	0.840 ± 0.010	0.861 ± 0.035	0.892 ± 0.017
GunPoint	0.984 ± 0.027	0.987 ± 0.007	**0.996** ± 0.004	0.987 ± 0.012	**0.996** ± 0.004
GunPointAgeSpan	0.980 ± 0.008	**0.998** ± 0.002	0.992 ± 0.002	0.993 ± 0.002	0.994 ± 0.000
GunPointMaleVersusFemale	**1.000** ± 0.000	0.999 ± 0.002	0.996 ± 0.002	**1.000** ± 0.000	**1.000** ± 0.000
GunPointOldVersusYoung	**1.000** ± 0.000	**1.000** ± 0.000	0.988 ± 0.002	**1.000** ± 0.000	**1.000** ± 0.000
Ham	**0.752** ± 0.025	0.667 ± 0.010	0.695 ± 0.000	0.721 ± 0.024	0.724 ± 0.019
HandOutlines	0.930 ± 0.007	0.931 ± 0.006	0.936 ± 0.007	**0.945** ± 0.010	0.932 ± 0.007
Haptics	0.491 ± 0.026	0.462 ± 0.002	0.498 ± 0.007	0.535 ± 0.040	**0.539** ± 0.009
Herring	**0.698** ± 0.018	0.682 ± 0.024	0.599 ± 0.009	0.630 ± 0.039	0.625 ± 0.027
HouseTwenty	0.947 ± 0.010	0.961 ± 0.010	0.972 ± 0.005	0.972 ± 0.010	**0.980** ± 0.005
InlineSkate	0.364 ± 0.019	0.334 ± 0.021	0.398 ± 0.015	0.401 ± 0.006	**0.408** ± 0.015
InsectEPGRegularTrain	0.987 ± 0.014	**1.000** ± 0.000	**1.000** ± 0.000	**1.000** ± 0.000	**1.000** ± 0.000

Continuation of Table 17

Dataset	Moment	Mantis	TiViT	TiViT + Moment	TiViT + Mantis
InsectEPGSmallTrain	0.953 ± 0.008	**1.000** ± 0.000	0.968 ± 0.007	0.973 ± 0.005	0.999 ± 0.002
InsectWingbeatSound	0.539 ± 0.003	0.470 ± 0.019	0.536 ± 0.015	**0.560** ± 0.007	0.539 ± 0.010
ItalyPowerDemand	**0.938** ± 0.005	0.910 ± 0.006	0.920 ± 0.018	0.936 ± 0.011	0.923 ± 0.018
LargeKitchenAppliances	0.859 ± 0.005	0.820 ± 0.010	**0.883** ± 0.014	0.873 ± 0.018	0.879 ± 0.014
Lightning2	0.760 ± 0.041	0.781 ± 0.025	0.803 ± 0.028	**0.820** ± 0.028	0.803 ± 0.016
Lightning7	0.836 ± 0.036	0.749 ± 0.021	0.831 ± 0.021	**0.881** ± 0.008	0.822 ± 0.024
Mallat	0.915 ± 0.010	0.868 ± 0.028	0.956 ± 0.017	**0.963** ± 0.016	0.958 ± 0.018
Meat	0.911 ± 0.038	**0.939** ± 0.019	0.800 ± 0.000	0.900 ± 0.029	0.850 ± 0.044
MedicalImages	0.730 ± 0.003	0.707 ± 0.024	0.740 ± 0.006	**0.780** ± 0.006	0.761 ± 0.014
MelbournePedestrian	**0.933** ± 0.003	0.908 ± 0.005	0.862 ± 0.006	0.932 ± 0.005	0.925 ± 0.003
MiddlePhalanxOutlineAgeGroup	0.489 ± 0.029	**0.587** ± 0.019	0.537 ± 0.036	0.530 ± 0.004	0.571 ± 0.023
MiddlePhalanxOutlineCorrect	0.816 ± 0.009	**0.845** ± 0.009	0.789 ± 0.015	0.792 ± 0.016	0.805 ± 0.016
MiddlePhalanxTW	0.506 ± 0.019	0.442 ± 0.017	0.506 ± 0.023	0.498 ± 0.025	**0.511** ± 0.010
MixedShapesRegularTrain	0.947 ± 0.004	0.955 ± 0.006	0.974 ± 0.002	0.973 ± 0.003	**0.976** ± 0.002
MixedShapesSmallTrain	0.882 ± 0.004	0.904 ± 0.002	0.950 ± 0.002	0.937 ± 0.004	**0.957** ± 0.003
MoteStrain	0.889 ± 0.028	0.895 ± 0.026	0.875 ± 0.021	**0.918** ± 0.008	0.901 ± 0.025
NonInvasiveFetalECGThorax1	0.919 ± 0.002	0.797 ± 0.006	0.884 ± 0.004	**0.924** ± 0.003	0.885 ± 0.009
NonInvasiveFetalECGThorax2	0.927 ± 0.002	0.817 ± 0.004	0.915 ± 0.001	**0.934** ± 0.004	0.918 ± 0.005
OSULeaf	0.917 ± 0.004	0.899 ± 0.005	0.977 ± 0.006	0.972 ± 0.010	**0.978** ± 0.009
OliveOil	**0.856** ± 0.051	0.822 ± 0.107	0.656 ± 0.077	0.778 ± 0.019	0.711 ± 0.051
PLAID	0.775 ± 0.017	0.852 ± 0.001	0.888 ± 0.008	0.901 ± 0.011	**0.928** ± 0.012
PhalangesOutlinesCorrect	**0.795** ± 0.006	0.794 ± 0.008	0.789 ± 0.004	**0.795** ± 0.008	0.787 ± 0.004
Phoneme	0.277 ± 0.003	0.293 ± 0.008	0.377 ± 0.006	0.372 ± 0.003	**0.386** ± 0.006
PickupGestureWiimoteZ	0.713 ± 0.042	0.767 ± 0.023	0.887 ± 0.031	0.847 ± 0.046	**0.893** ± 0.023
PigAirwayPressure	0.109 ± 0.007	0.588 ± 0.012	0.540 ± 0.006	0.447 ± 0.013	**0.598** ± 0.010
PigArtPressure	0.780 ± 0.010	0.827 ± 0.017	0.817 ± 0.013	0.833 ± 0.019	**0.846** ± 0.005
PigCVP	0.747 ± 0.027	0.753 ± 0.007	0.702 ± 0.019	0.761 ± 0.018	**0.801** ± 0.012
Plane	0.997 ± 0.005	**1.000** ± 0.000	**1.000** ± 0.000	**1.000** ± 0.000	**1.000** ± 0.000
PowerCons	0.931 ± 0.006	0.933 ± 0.010	0.894 ± 0.022	**0.943** ± 0.013	0.906 ± 0.020
ProximalPhalanxOutlineAgeGroup	0.802 ± 0.020	**0.852** ± 0.007	0.833 ± 0.027	0.824 ± 0.005	0.828 ± 0.017
ProximalPhalanxOutlineCorrect	0.883 ± 0.010	**0.885** ± 0.008	0.861 ± 0.020	0.871 ± 0.016	0.858 ± 0.023
ProximalPhalanxTW	**0.767** ± 0.010	0.740 ± 0.015	0.751 ± 0.022	0.730 ± 0.010	0.759 ± 0.023
RefrigerationDevices	0.496 ± 0.017	0.526 ± 0.022	0.555 ± 0.007	0.531 ± 0.005	**0.570** ± 0.014
Rock	0.727 ± 0.031	0.700 ± 0.060	**0.873** ± 0.099	**0.873** ± 0.115	0.853 ± 0.117
ScreenType	0.499 ± 0.020	0.468 ± 0.026	0.530 ± 0.014	0.516 ± 0.002	**0.552** ± 0.027
SemgHandGenderCh2	0.761 ± 0.018	0.883 ± 0.006	0.879 ± 0.001	0.878 ± 0.013	**0.914** ± 0.006
SemgHandMovementCh2	0.398 ± 0.010	0.654 ± 0.018	0.545 ± 0.016	0.538 ± 0.031	**0.688** ± 0.024
SemgHandSubjectCh2	0.648 ± 0.013	0.826 ± 0.005	0.840 ± 0.002	0.838 ± 0.012	**0.895** ± 0.007
ShakeGestureWiimoteZ	0.887 ± 0.012	0.867 ± 0.012	0.827 ± 0.031	**0.907** ± 0.031	0.840 ± 0.020
ShapeletSim	0.967 ± 0.010	0.919 ± 0.012	**1.000** ± 0.000	**1.000** ± 0.000	**1.000** ± 0.000
ShapesAll	0.886 ± 0.003	0.844 ± 0.010	0.901 ± 0.003	**0.913** ± 0.008	0.908 ± 0.007
SmallKitchenAppliances	0.733 ± 0.010	0.796 ± 0.013	**0.830** ± 0.003	0.817 ± 0.018	0.812 ± 0.008
SmoothSubspace	0.898 ± 0.023	**0.971** ± 0.004	0.956 ± 0.010	0.964 ± 0.010	**0.971** ± 0.010
SonyAIBORobotSurface1	0.834 ± 0.013	0.858 ± 0.015	0.890 ± 0.012	0.869 ± 0.009	**0.896** ± 0.010
SonyAIBORobotSurface2	0.855 ± 0.027	0.895 ± 0.012	0.911 ± 0.049	0.914 ± 0.049	**0.923** ± 0.048
StarLightCurves	0.969 ± 0.003	0.968 ± 0.002	0.973 ± 0.002	**0.976** ± 0.002	**0.976** ± 0.002
Strawberry	**0.972** ± 0.002	0.960 ± 0.004	0.959 ± 0.002	0.968 ± 0.006	0.959 ± 0.003
SwedishLeaf	0.915 ± 0.007	0.942 ± 0.006	0.955 ± 0.003	**0.959** ± 0.006	0.958 ± 0.003
Symbols	0.957 ± 0.019	0.957 ± 0.031	0.966 ± 0.034	**0.973** ± 0.020	0.967 ± 0.035
SyntheticControl	0.966 ± 0.004	0.992 ± 0.002	0.999 ± 0.002	0.993 ± 0.003	**1.000** ± 0.000
ToeSegmentation1	**0.963** ± 0.007	0.952 ± 0.012	0.952 ± 0.012	**0.963** ± 0.005	0.959 ± 0.009
ToeSegmentation2	0.885 ± 0.015	**0.954** ± 0.008	0.923 ± 0.008	0.895 ± 0.027	0.926 ± 0.004
Trace	**1.000** ± 0.000	**1.000** ± 0.000	**1.000** ± 0.000	**1.000** ± 0.000	**1.000** ± 0.000
TwoLeadECG	0.901 ± 0.020	0.998 ± 0.002	0.997 ± 0.001	0.997 ± 0.001	**1.000** ± 0.000
TwoPatterns	0.989 ± 0.001	0.946 ± 0.007	0.998 ± 0.000	**0.999** ± 0.001	0.998 ± 0.001
UMD	**0.993** ± 0.000	**0.993** ± 0.000	**0.993** ± 0.000	**0.993** ± 0.000	**0.993** ± 0.000
UWaveGestureLibraryAll	0.923 ± 0.002	0.874 ± 0.004	0.940 ± 0.001	**0.950** ± 0.005	0.944 ± 0.003
UWaveGestureLibraryX	0.792 ± 0.001	0.779 ± 0.004	0.828 ± 0.004	**0.838** ± 0.004	**0.838** ± 0.002
UWaveGestureLibraryY	0.711 ± 0.006	0.678 ± 0.009	0.749 ± 0.004	0.758 ± 0.004	**0.763** ± 0.006
UWaveGestureLibraryZ	0.731 ± 0.001	0.742 ± 0.009	0.770 ± 0.003	0.772 ± 0.004	**0.786** ± 0.001
Wafer	0.992 ± 0.002	0.996 ± 0.000	**1.000** ± 0.000	**1.000** ± 0.000	**1.000** ± 0.000
Wine	**0.889** ± 0.019	0.796 ± 0.037	0.599 ± 0.065	0.747 ± 0.028	0.759 ± 0.049
WordSynonyms	0.655 ± 0.003	0.626 ± 0.017	0.649 ± 0.007	**0.690** ± 0.005	0.681 ± 0.006
Worms	0.745 ± 0.033	0.710 ± 0.033	0.762 ± 0.027	**0.805** ± 0.026	0.762 ± 0.052
WormsTwoClass	0.775 ± 0.037	0.745 ± 0.007	0.784 ± 0.020	**0.792** ± 0.026	0.766 ± 0.022
Yoga	0.833 ± 0.008	0.771 ± 0.014	0.826 ± 0.009	**0.852** ± 0.007	0.844 ± 0.007

End of Table

Table 18: Classification accuracy for 27 multivariate datasets from the UEA benchmark. We report the mean and standard deviation across three random seeds.

Dataset	Moment	Mantis	TiViT	TiViT + Moment	TiViT + Mantis
ArticularyWordRecognition	0.988 ± 0.002	**0.991** ± 0.002	0.977 ± 0.003	0.977 ± 0.003	0.974 ± 0.005
BasicMotions	**1.000** ± 0.000	**1.000** ± 0.000	**1.000** ± 0.000	**1.000** ± 0.000	**1.000** ± 0.000
CharacterTrajectories	**0.982** ± 0.001	0.973 ± 0.001	0.964 ± 0.005	**0.982** ± 0.001	0.978 ± 0.005
Cricket	**1.000** ± 0.000	0.986 ± 0.000	**1.000** ± 0.000	**1.000** ± 0.000	**1.000** ± 0.000
DuckDuckGeese	**0.467** ± 0.081	0.433 ± 0.023	0.393 ± 0.081	0.413 ± 0.064	0.433 ± 0.050
ERing	0.895 ± 0.022	0.905 ± 0.025	0.975 ± 0.014	0.977 ± 0.006	**0.981** ± 0.007
EigenWorms	0.746 ± 0.022	0.746 ± 0.016	**0.911** ± 0.016	0.880 ± 0.009	**0.911** ± 0.012
Epilepsy	**1.000** ± 0.000	0.990 ± 0.004	**1.000** ± 0.000	**1.000** ± 0.000	**1.000** ± 0.000
EthanolConcentration	0.445 ± 0.013	0.269 ± 0.044	**0.485** ± 0.012	0.473 ± 0.030	0.465 ± 0.019
FaceDetection	0.584 ± 0.007	0.592 ± 0.006	0.598 ± 0.004	0.584 ± 0.007	**0.607** ± 0.005
FingerMovements	**0.633** ± 0.045	0.593 ± 0.025	0.517 ± 0.040	0.620 ± 0.036	0.553 ± 0.050
HandMovementDirection	**0.279** ± 0.051	0.212 ± 0.021	0.275 ± 0.016	0.257 ± 0.036	0.257 ± 0.027
Handwriting	0.296 ± 0.018	**0.425** ± 0.013	0.307 ± 0.034	0.340 ± 0.002	0.385 ± 0.021
Heartbeat	0.735 ± 0.007	**0.800** ± 0.017	0.732 ± 0.008	0.717 ± 0.022	0.769 ± 0.003
InsectWingbeat	0.231 ± 0.012	**0.573** ± 0.017	0.355 ± 0.008	0.332 ± 0.018	0.443 ± 0.020
JapaneseVowels	0.918 ± 0.006	**0.978** ± 0.003	0.940 ± 0.002	0.938 ± 0.012	0.933 ± 0.008
LSST	0.571 ± 0.005	0.607 ± 0.009	0.604 ± 0.005	0.610 ± 0.009	**0.652** ± 0.003
Libras	0.861 ± 0.017	0.887 ± 0.026	0.907 ± 0.006	**0.922** ± 0.022	0.920 ± 0.018
MotorImagery	0.530 ± 0.026	**0.563** ± 0.012	**0.563** ± 0.049	0.560 ± 0.044	0.553 ± 0.042
NATOPS	0.900 ± 0.029	**0.931** ± 0.014	0.869 ± 0.006	0.889 ± 0.006	0.878 ± 0.006
PEMS-SF	0.705 ± 0.029	**0.788** ± 0.029	0.709 ± 0.084	0.763 ± 0.044	0.742 ± 0.087
PhonemeSpectra	0.186 ± 0.004	0.272 ± 0.006	0.245 ± 0.007	0.265 ± 0.007	**0.286** ± 0.008
RacketSports	0.829 ± 0.007	**0.919** ± 0.004	0.846 ± 0.010	0.871 ± 0.008	0.879 ± 0.027
SelfRegulationSCP1	0.762 ± 0.010	0.825 ± 0.022	0.858 ± 0.008	0.840 ± 0.003	**0.891** ± 0.010
SelfRegulationSCP2	0.509 ± 0.031	0.491 ± 0.018	**0.526** ± 0.038	0.506 ± 0.017	0.517 ± 0.020
SpokenArabicDigits	**0.981** ± 0.003	0.907 ± 0.006	0.969 ± 0.001	0.979 ± 0.003	0.972 ± 0.002
UWaveGestureLibrary	0.846 ± 0.010	0.879 ± 0.015	0.910 ± 0.005	0.902 ± 0.004	**0.919** ± 0.009

Table 19: Mean rank of TiViT and TSFMs across datasets from the UCR and UEA archive.

Model	UCR	UEA
Moment	3.75	3.33
Mantis	3.43	2.85
TiViT *(Ours)*	2.97	2.85
TiViT + Moment *(Ours)*	2.20	2.63
TiViT + Mantis *(Ours)*	**1.95**	**2.22**

F BROADER IMPACTS

Since this paper presents foundational machine learning research, we do not see any direct societal risks. The broader impact of our work will depend on its specific application.

We demonstrate that our method TiViT significantly improves classification accuracy. This advancement can be beneficial in healthcare where the analysis of physiological signals is crucial for early diagnosis and treatment or in industry where the accurate monitoring of sensor data enables predictive maintenance and reduces downtime.

However, deep learning models including TiViT operate as black boxes with limited interpretability. In safety-critical domains or applications directly impacting humans, such models necessitate careful deployment and oversight. Further research into interpretability and human-in-the-loop frameworks is essential to make deep learning models trustworthy for real-world settings.

Table 20: Classification accuracy across 91 UCR datasets. Baselines from Goswami et al. (2024).

Accuracy	TiViT + Mantis	TiViT	Mantis	MOMENT	TimesNet	GPT4TS	TS2Vec	T-Loss	TNC	TS-TCC
Mean	0.848	0.834	0.826	0.794	0.572	0.566	**0.851**	0.833	0.786	0.793
Median	**0.880**	0.849	0.852	0.815	0.565	0.583	0.871	0.849	0.788	0.802
Std.	0.133	0.136	0.143	0.147	0.238	0.234	0.134	0.136	0.168	0.176

Accuracy	TST	CNN	Encoder	FCN	MCNN	MLP	ResNet	t-LeNet	TWIESN	DTW
Mean	0.658	0.751	0.743	0.809	0.702	0.750	0.825	0.348	0.726	0.764
Median	0.720	0.773	0.753	0.837	0.718	0.766	0.852	0.333	0.724	0.768
Std.	0.220	0.180	0.159	0.188	0.194	0.169	0.177	0.221	0.164	0.152

Table 21: Classification accuracy across 29 UEA datasets. Baselines from Goswami et al. (2024).

Accuracy	TiViT + Mantis	TiViT	Mantis	MOMENT	TS2Vec	T-Loss	TNC	TS-TCC	TST	DTW
Mean	**71.9**	70.6	69.3	0.670	0.694	0.646	0.660	0.657	0.605	0.638
Median	**82.3**	78.9	78.8	0.722	0.683	0.676	0.746	0.751	0.620	0.664
Std.	26.0	26.6	26.6	0.274	0.255	0.296	0.267	0.263	0.294	0.296

Method		**Pretraining + linear probing**						**Supervised training**											
		TiViT (Ours)		**MOMENT**		**GPT4TS**		**PatchTST**		**DLinear**		**TimesNet**		**FEDFormer**		**Stationary**		**N-BEATS**	
Metric		MSE	MAE	MSE	MAE	MSE	MAE	MSE	MAE	MSE	MAE	MSE	MAE	MSE	MAE	MSE	MAE	MSE	MAE
Weather	96	0.153	0.211	0.154	0.209	0.162	0.212	0.149	0.198	0.176	0.237	0.172	0.220	0.217	0.296	0.173	0.223	0.152	0.210
	192	0.196	0.247	0.197	0.248	0.204	0.248	0.194	0.241	0.220	0.282	0.219	0.261	0.276	0.336	0.245	0.285	0.199	0.260
	336	0.248	0.285	0.246	0.285	0.254	0.286	0.245	0.282	0.265	0.319	0.280	0.306	0.339	0.380	0.321	0.338	0.258	0.311
	720	0.321	0.337	0.315	0.336	0.326	0.337	0.314	0.334	0.333	0.362	0.365	0.359	0.403	0.428	0.414	0.410	0.331	0.359
ECL	96	0.140	0.240	0.136	0.233	0.139	0.238	0.129	0.222	0.140	0.237	0.168	0.272	0.193	0.308	0.169	0.273	0.131	0.228
	192	0.152	0.251	0.152	0.247	0.153	0.251	0.157	0.240	0.153	0.249	0.184	0.289	0.201	0.315	0.182	0.286	0.153	0.248
	336	0.168	0.267	0.167	0.264	0.169	0.266	0.163	0.259	0.169	0.267	0.198	0.300	0.214	0.329	0.200	0.304	0.170	0.267
	720	0.204	0.297	0.205	0.295	0.206	0.297	0.197	0.290	0.203	0.301	0.220	0.320	0.246	0.355	0.222	0.321	0.208	0.298
Traffic	96	0.384	0.274	0.391	0.282	0.388	0.282	0.360	0.249	0.410	0.282	0.593	0.321	0.587	0.366	0.612	0.338	0.375	0.259
	192	0.398	0.280	0.404	0.287	0.407	0.290	0.379	0.256	0.423	0.287	0.617	0.336	0.604	0.373	0.613	0.340	0.403	0.274
	336	0.407	0.285	0.414	0.292	0.412	0.294	0.392	0.264	0.436	0.296	0.629	0.336	0.621	0.383	0.618	0.328	0.426	0.285
	720	0.443	0.303	0.450	0.310	0.450	0.312	0.432	0.286	0.466	0.315	0.640	0.350	0.626	0.382	0.653	0.355	0.508	0.335
ETTh1	96	0.391	0.417	0.387	0.410	0.376	0.397	0.370	0.399	0.375	0.399	0.384	0.402	0.376	0.419	0.513	0.491	0.399	0.428
	192	0.411	0.430	0.410	0.426	0.416	0.418	0.413	0.421	0.405	0.416	0.436	0.429	0.420	0.448	0.534	0.504	0.451	0.464
	336	0.425	0.442	0.422	0.437	0.442	0.433	0.422	0.436	0.439	0.443	0.491	0.469	0.459	0.465	0.588	0.535	0.498	0.500
	720	0.447	0.469	0.454	0.472	0.477	0.456	0.447	0.466	0.472	0.490	0.521	0.500	0.506	0.507	0.643	0.616	0.608	0.573
ETTh2	96	0.319	0.375	0.288	0.345	0.285	0.342	0.274	0.336	0.289	0.353	0.340	0.374	0.358	0.397	0.476	0.458	0.327	0.387
	192	0.363	0.406	0.349	0.386	0.354	0.389	0.339	0.379	0.383	0.418	0.402	0.414	0.429	0.439	0.512	0.493	0.400	0.435
	336	0.372	0.418	0.369	0.408	0.373	0.407	0.329	0.380	0.448	0.465	0.452	0.452	0.496	0.487	0.552	0.551	0.747	0.599
	720	0.407	0.447	0.403	0.439	0.406	0.441	0.379	0.422	0.605	0.551	0.462	0.468	0.463	0.474	0.562	0.560	1.454	0.847
ETTm1	96	0.315	0.367	0.293	0.349	0.292	0.346	0.290	0.342	0.299	0.343	0.338	0.375	0.379	0.419	0.386	0.398	0.318	0.367
	192	0.352	0.387	0.326	0.368	0.332	0.372	0.332	0.369	0.335	0.365	0.374	0.387	0.426	0.441	0.459	0.444	0.355	0.391
	336	0.381	0.404	0.352	0.384	0.366	0.394	0.366	0.392	0.369	0.386	0.410	0.411	0.445	0.459	0.495	0.464	0.401	0.419
	720	0.437	0.436	0.405	0.416	0.417	0.421	0.416	0.420	0.425	0.421	0.478	0.450	0.543	0.490	0.585	0.516	0.448	0.448
ETTm2	96	0.189	0.277	0.170	0.260	0.173	0.262	0.165	0.255	0.167	0.269	0.187	0.267	0.203	0.287	0.192	0.274	0.197	0.271
	192	0.252	0.318	0.227	0.297	0.229	0.301	0.220	0.292	0.224	0.303	0.249	0.309	0.269	0.328	0.280	0.339	0.285	0.328
	336	0.301	0.351	0.275	0.328	0.286	0.341	0.274	0.329	0.281	0.342	0.321	0.351	0.325	0.366	0.334	0.361	0.338	0.366
	720	0.382	0.405	0.363	0.387	0.378	0.401	0.362	0.385	0.397	0.421	0.408	0.403	0.421	0.415	0.417	0.413	0.395	0.419
ILI	24	2.822	1.142	2.728	1.114	2.063	0.881	1.319	0.754	2.215	1.081	2.317	0.934	3.228	1.260	2.294	0.945	4.539	1.528
	36	2.862	1.143	2.669	1.092	1.868	0.892	1.430	0.834	1.963	0.963	1.972	0.920	2.679	1.080	1.825	0.848	4.628	1.534
	48	2.846	1.123	2.728	1.098	1.790	0.884	1.553	0.815	2.130	1.024	2.238	0.940	2.622	1.078	2.010	0.900	4.957	1.585
	60	3.023	1.155	2.883	1.126	1.979	0.957	1.470	0.788	2.368	1.096	2.027	0.928	2.857	1.157	2.178	0.963	5.429	1.661

Table 22: Long-term forecasting. Baselines from Goswami et al. (2024).

	Adjusted Best F_1					VUS-ROC				
	TiViT	Anomaly TF	Moment	GPT4TS	TimesNet	TiViT	AnomalyTF	Moment	GPT4TS	TimesNet
1sddb40	**0.935**	0.030	0.540	0.190	0.680	**0.772**	0.640	0.750	0.660	0.720
BIDMC1	**1.000**	0.990	**1.000**	**1.000**	**1.000**	0.642	0.690	0.650	0.630	**0.740**
CHARISfive	0.046	0.010	**0.130**	0.020	0.080	**0.572**	0.360	0.400	0.450	0.460
CHARISten	**0.851**	0.020	0.110	0.100	0.030	**0.597**	0.430	0.540	0.510	0.530
CIMIS44AirTemperature3	**1.000**	0.060	0.980	0.180	0.470	**0.843**	0.640	0.750	0.620	0.740
CIMIS44AirTemperature5	**1.000**	0.390	0.990	0.200	0.710	**0.859**	0.780	0.810	0.560	0.720
ECG2	**1.000**	**1.000**	**1.000**	0.900	**1.000**	0.821	0.830	**0.840**	0.780	0.600
ECG3	**1.000**	0.360	0.980	0.840	0.480	**0.808**	0.540	0.770	0.450	0.610
Fantasia	**1.000**	0.750	0.950	0.870	0.550	**0.786**	0.730	0.640	0.650	0.610
GP711MarkerLFM5z4	**1.000**	0.930	**1.000**	0.640	0.950	**0.886**	0.540	0.730	0.620	0.720
GP711MarkerLFM5z5	**1.000**	0.760	0.970	0.480	0.900	**0.961**	0.690	0.720	0.630	0.840
InternalBleeding5	**1.000**	0.940	**1.000**	0.920	**1.000**	0.932	0.460	0.690	0.630	**0.940**
Italianpowerdemand	0.310	0.010	**0.740**	0.010	0.440	0.709	0.450	**0.770**	0.480	0.710
Lab2Cmac011215EPG5	**1.000**	0.990	0.980	0.600	0.990	0.739	**0.770**	0.630	0.640	0.610
Lab2Cmac011215EPG6	0.267	**0.410**	0.100	0.100	0.170	0.554	**0.700**	0.480	0.520	0.450
MesoplodonDensirostris	**1.000**	**1.000**	0.840	**1.000**	**1.000**	0.748	**0.850**	0.720	0.690	0.790
PowerDemand1	**0.994**	0.870	0.440	0.760	0.950	**0.919**	0.720	0.540	0.600	0.750
TkeepFirstMARS	**0.577**	0.010	0.150	0.020	0.230	0.728	0.520	0.760	0.500	**0.790**
TkeepSecondMARS	**1.000**	0.830	**1.000**	0.120	0.950	**0.989**	0.720	0.910	0.810	0.980
WalkingAceleration5	0.967	0.990	**1.000**	0.870	0.930	**0.968**	0.940	0.870	0.910	0.850
apneaecg	**0.814**	0.400	0.200	0.310	0.260	0.608	0.580	0.690	0.580	**0.760**
apneaecg2	**1.000**	0.650	**1.000**	**1.000**	0.650	**0.845**	0.790	0.740	0.650	0.610
gait1	**1.000**	0.180	0.360	0.410	0.520	**0.887**	0.630	0.570	0.580	0.600
gaitHunt1	**0.596**	0.080	0.430	0.100	0.300	**0.847**	0.810	0.680	0.710	0.840
insectEPG2	**0.962**	0.120	0.230	0.810	0.960	**0.871**	0.650	0.820	0.560	0.730
insectEPG4	0.513	0.980	**1.000**	0.210	0.850	0.691	0.690	**0.720**	0.490	0.650
ltstdbs30791AS	**1.000**	**1.000**	**1.000**	**1.000**	**1.000**	**0.959**	0.780	0.810	0.740	0.670
mit14046longtermecg	**0.676**	0.450	0.590	0.580	0.600	0.661	0.790	0.660	0.610	**0.840**
park3m	**1.000**	0.150	0.640	0.630	0.930	**0.875**	0.630	0.780	0.540	0.780
qtdbSel1005V	**0.844**	0.410	0.650	0.390	0.530	0.612	0.520	**0.640**	0.610	0.540
qtdbSel100MLII	**1.000**	0.420	0.840	0.600	0.870	0.573	0.620	0.620	0.580	**0.650**
resperation1	**0.308**	0.000	0.150	0.010	0.030	0.725	**0.750**	0.670	0.470	0.670
s20101mML2	**1.000**	0.690	0.710	0.050	0.080	**0.942**	0.640	0.720	0.640	0.690
sddb49	**1.000**	0.890	**1.000**	0.940	**1.000**	**0.937**	0.660	0.730	0.580	0.680
sel840mECG1	**0.984**	0.160	0.660	0.210	0.360	0.702	0.620	**0.720**	0.650	0.600
sel840mECG2	**0.984**	0.150	0.390	0.280	0.210	0.683	0.590	**0.690**	0.520	0.520
tilt12744mtable	**0.254**	0.070	0.240	0.000	0.030	**0.761**	0.480	0.740	0.510	0.640
tilt12754table	0.131	0.230	**0.640**	0.060	0.050	**0.855**	0.600	0.820	0.550	0.750
tiltAPB2	**1.000**	0.920	0.980	0.830	0.380	**0.844**	0.770	0.770	0.600	0.700
tiltAPB3	0.148	0.170	**0.850**	0.050	0.090	**0.769**	0.680	0.650	0.440	0.580
weallwalk	**0.706**	0.000	0.580	0.130	0.170	0.849	0.730	**0.930**	0.870	0.850
Mean	**0.802**	0.475	0.684	0.449	0.570	**0.789**	0.659	0.711	0.605	0.695
Median	**0.994**	0.410	0.740	0.390	0.550	**0.808**	0.660	0.720	0.600	0.700
Std	0.300	0.379	0.321	0.358	0.355	0.122	0.124	0.106	0.107	0.118

Table 23: Anomaly detection performance across 41 datasets from the UCR Anomaly Archive measured using adjusted best F_1 and VUS-ROC. Bold indicates the best performance per dataset/metric. Baselines from Goswami et al. (2024).